Hele-Shaw flow of a nematic liquid crystal

Joseph R. L. Cousins [1,2,*] Nigel J. Mottram [2,†] and Stephen K. Wilson [1,‡]

[1]*Department of Mathematics and Statistics, University of Strathclyde,*
Livingstone Tower, 26 Richmond Street, Glasgow G1 1XH, United Kingdom
[2]*School of Mathematics and Statistics, University of Glasgow, University Place, Glasgow G12 8QQ, United Kingdom*

Motivated by the variety of applications in which nematic Hele-Shaw flow occurs, a theoretical model for Hele-Shaw flow of a nematic liquid crystal is formulated and analyzed. We derive the thin-film Ericksen-Leslie equations that govern nematic Hele-Shaw flow, and consider two important limiting cases in which we can make significant analytical progress. First, we consider the leading-order problem in the limiting case in which elasticity effects dominate viscous effects, and find that the nematic liquid crystal anchoring on the plates leads to a fixed director field and an anisotropic patterned viscosity that can be used to guide the flow of the nematic. Second, we consider the leading-order problem in the opposite limiting case in which viscous effects dominate elasticity effects, and find that the flow is identical to that of an isotropic fluid and the behavior of the director is determined by the flow. As an example of the insight which can be gained by using the present approach, we then consider the flow of nematic according to a simple model for the squeezing stage of the one-drop-filling method, an important method for the manufacture of liquid crystal displays, in these two limiting cases.

I. INTRODUCTION

Following the original experiments by Hele-Shaw [1] and the pioneering theory for the flow of a viscous fluid by Stokes [2], interest in what is now termed Hele-Shaw flow has remained the subject of ongoing research for well over a century. What is now called a Hele-Shaw cell consists of two parallel plates separated by a narrow gap which is partially or wholly filled with viscous fluid. Mathematically, this system naturally lends itself to a thin-film (i.e., a lubrication) analysis, and significant progress is often possible using analytical methods and reduced models that are computationally much cheaper than fully numerical alternatives [3]. Experimentally, Hele-Shaw cells are a useful tool for visualizing two-dimensional flows that have allowed researchers to investigate many fluid mechanical effects. Such effects include viscous fingering [4,5], porosity [6–8], and bubble dynamics [9,10]. An extensive list of work up to 1998 that details many of the applications of isotropic Hele-Shaw cells is available at [11], and a more up-to-date review of Hele-Shaw flow is given by Morrow *et al.* [12].

Although much of the work on Hele-Shaw flow has focused on isotropic fluids, there has also been some interest

in the Hele-Shaw flow of non-Newtonian fluids, including the flow of power-law fluids by Hassager and Lauridsen [13] and the flow of viscoelastic fluids by Ro and Homsy [14]. Somewhat surprisingly, there has been little work on the theory of Hele-Shaw cells filled with liquid crystals, despite their relevance to the liquid crystal display (LCD) industry, in which thin-film flows of liquid crystal between parallel plates are a key element of device manufacture [15]. Liquid crystals are anisotropic fluids with long-range molecular orientational order and possibly molecular positional order that exhibit a rich variety of physical behaviors, including anisotropic elasticity, viscosity, and surface effects [16]. The appearance of long-range order can occur as the temperature changes, in which case the phase is termed a thermotropic liquid crystal, or as the concentration of a solvent in a solute changes, in which case the phase is termed a lyotropic liquid crystal. The most common type of liquid crystal used in LCDs are thermotropic nematic liquid crystals, which in the present work we term nematics, which exhibit orientational order but no positional order. The standard continuum approach used to mathematically model the behavior of nematics makes use of the so-called director $\boldsymbol{n}$, a unit vector representing the average nematic molecular orientation, together with the fluid velocity $\boldsymbol{u}$ and fluid pressure p, to formulate the conservation of mass equation, the conservation of linear momentum equations, and the conservation of angular momentum equations. These conservation equations are known as the Ericksen-Leslie equations [17,18], and they have been successfully applied to a variety of problems involving the flow of nematics [16,19].

Although there has been only limited theoretical study of nematic Hele-Shaw flow, there has been some experimental work on nematic viscous fingering [20–23], some of which has included simple theoretical models [22,23]. For example,

---

*Contact author: joseph.cousins@strath.ac.uk
†Contact author: nigel.mottram@glasgow.ac.uk
‡Present address: Department of Mathematical Sciences, University of Bath, Claverton Down, Bath BA2 7AY, United Kingdom;
Contact author: s.k.wilson@strath.ac.uk

Lam *et al.* [22] consider a number of fixed director fields for which the flow of a nematic is identical to the flow of an isotropic fluid with effective viscosity determined by the fixed director field. Following the initial experiments on nematic viscous fingering by Buka *et al.* [20] and Sonin and Bartolino [21], there have been a variety of extensions of this work, for example, to the viscous fingering of nematics under applied electric fields by Folch *et al.* [24,25] and Tóth-Katona and Buka [26]. Nematic microfluidic experiments have also been the topic of much recent interest [27]; in particular, experiments by Sengupta *et al.* [28–30] have inspired work on a variety of effects, including control of nematic defects [31–33], micropillar induced cavitation [34,35], and control of nematic flow using external stimuli [36,37]. These experiments have also initiated a number of theoretical investigations. For example, flow transitions observed by Sengupta *et al.* [28–30] have been studied using the Ericksen-Leslie equations by Anderson *et al.* [38] and Crespo *et al.* [39] and using lattice Boltzmann simulations by Batista *et al.* [40]. However, many of these studies employ one-dimensional models for the nematic that cannot capture two-dimensional effects. Although in the present work we focus on nematics, a similar approach may also be useful for the study of lyotropic microfluidics [41,42].

As previously mentioned, Hele-Shaw flow is particularly relevant to the industrial manufacture of LCDs, which involves filling the gap between parallel plates with nematic [43]. LCD manufacturing is currently carried out using one of two methods: the capillary-filling method and the one-drop-filling (ODF) method [44]. In the capillary-filling method, the nematic is introduced at one edge of the parallel plates and fills the gap between the plates via capillary action, which results in relatively low flow speeds and long manufacturing times [15]. In the ODF method, an array of nematic droplets are dispensed on one plate, and a second (parallel) plate is lowered onto droplets, squeezing them until they coalesce to form a continuous nematic film between the plates, which results in relatively high flow speeds and short manufacturing times [44]. The ODF method is often preferred because of this higher manufacturing throughput of devices when compared to the capillary-filling method. However, the ODF method can sometimes lead to unwanted optical effects, known as ODF mura, which degrade the quality of the final display [45–47]. Somewhat surprisingly, there has been relatively little work to model the nematic flow in these manufacturing methods using the standard theoretical approach for isotropic Hele-Shaw flow [3]. For further discussion of nematic flow in LCD manufacturing see Cousins *et al.* [48–50].

Motivated by the variety of applications in which nematic Hele-Shaw flow occurs, in the present work we formulate and analyze a theoretical model for Hele-Shaw flow of a nematic liquid crystal. In Secs. II to VII, we derive the thin-film Ericksen-Leslie equations that govern nematic Hele-Shaw flow. Then, we consider these equations in a number of important limiting cases in which we can make significant analytical progress. First, in Sec. VIII, we consider the leading-order problem in the limiting case in which elasticity effects dominate viscous effects and, second, in Sec. IX, we consider the leading-order problem in the opposite limiting case in which viscous effects dominate elasticity effects. Finally, in Sec. X,
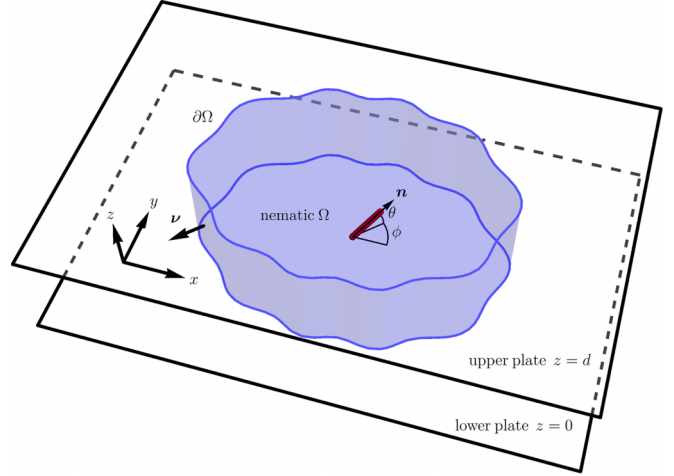

FIG. 1. A Hele-Shaw cell showing a perspective view of a region of nematic Ω (in light blue) bounded between solid parallel plates at $z = 0$ and $z = d$, and with a free surface $\partial\Omega$ with outward unit normal $\boldsymbol{\nu}$. The Cartesian coordinates x, y, and z, the director $\boldsymbol{n}$, the tilt director angle θ, and the twist director angle ϕ are also shown.

as an example of the insight which can be gained by using the present approach, we consider the flow of nematic according to a simple model for the squeezing stage of the ODF method in these two limiting cases.

II. PROBLEM FORMULATION

We consider the flow of a nematic in a standard Hele-Shaw cell that consists of two parallel plates separated by a narrow gap which is partially or wholly filled with the nematic. In particular, we consider a region of nematic $\Omega = \Omega(t)$ bounded between solid parallel plates at $z = 0$ (which we term the lower plate) and $z = d(t)$ (which we term the upper plate), and with a free surface $\partial\Omega = \partial\Omega(t)$ with outward unit normal $\boldsymbol{\nu} = \boldsymbol{\nu}(x, y, z, t)$, where x, y, and z are Cartesian coordinates, t denotes time, as shown in Fig. 1. Note that the thickness of the cell in the z direction, $d(t)$, may, in general, be time dependent, and so we allow for the possibility of the upper plate to move in the direction perpendicular to the plates, with the velocity of the upper plate denoted by $d' = d'(t)$. (Note that, despite what Fig. 1 might suggest, in the following mathematical model it is not necessary for the region of nematic to be simply connected.) The nematic velocity and the fluid pressure are denoted by

$$\boldsymbol{u} = u(x, y, z, t)\hat{\boldsymbol{x}} + v(x, y, z, t)\hat{\boldsymbol{y}} + w(x, y, z, t)\hat{\boldsymbol{z}}, \quad (1)$$

$$p = p(x, y, z, t), \quad (2)$$

respectively, where $\hat{\boldsymbol{x}}$, $\hat{\boldsymbol{y}}$, and $\hat{\boldsymbol{z}}$ are the Cartesian coordinate unit vectors in the x, y, and z directions and u, v, and w are the components of the velocity in the x, y, and z directions. The director $\boldsymbol{n} = \boldsymbol{n}(x, y, z, t)$ is written in the form

$$\boldsymbol{n} = \cos\theta(x, y, z, t)\cos\phi(x, y, z, t)\hat{\boldsymbol{x}}$$
$$+ \cos\theta(x, y, z, t)\sin\phi(x, y, z, t)\hat{\boldsymbol{y}} + \sin\theta(x, y, z, t)\hat{\boldsymbol{z}}, \quad (3)$$

where $\theta(x, y, z, t)$ is the angle between the director and the xy plane, which is commonly called the tilt director angle, and $\phi(x, y, z, t)$ is the angle between the projection of the director onto the xy plane and the x axis, which is commonly called the twist director angle [16].

III. THE GOVERNING EQUATIONS

In this work we consider governing equations for the velocity, pressure and director in the form of the Ericksen-Leslie equations [17,18], which are derived from a continuum approach and the principles of the conservation of mass, the conservation of linear momentum, and the conservation of angular momentum.

The conservation of mass equation is given by

$$\frac{\partial u}{\partial x} + \frac{\partial v}{\partial y} + \frac{\partial w}{\partial z} = 0. \tag{4}$$

The conservation of linear momentum equations are given by

$$\rho \dot{u} = -\frac{\partial \tilde{p}}{\partial x} + \frac{\partial}{\partial x}\left(\frac{\partial \mathcal{D}}{\partial u_x}\right) + \frac{\partial}{\partial y}\left(\frac{\partial \mathcal{D}}{\partial u_y}\right) + \frac{\partial}{\partial z}\left(\frac{\partial \mathcal{D}}{\partial u_z}\right) \\ - \frac{\partial \mathcal{D}}{\partial \theta}\frac{\partial \theta}{\partial x} - \frac{\partial \mathcal{D}}{\partial \phi}\frac{\partial \phi}{\partial x}, \tag{5}$$

$$\rho \dot{v} = -\frac{\partial \tilde{p}}{\partial y} + \frac{\partial}{\partial x}\left(\frac{\partial \mathcal{D}}{\partial v_x}\right) + \frac{\partial}{\partial y}\left(\frac{\partial \mathcal{D}}{\partial v_y}\right) + \frac{\partial}{\partial z}\left(\frac{\partial \mathcal{D}}{\partial v_z}\right) \\ - \frac{\partial \mathcal{D}}{\partial \theta}\frac{\partial \theta}{\partial y} - \frac{\partial \mathcal{D}}{\partial \phi}\frac{\partial \phi}{\partial y}, \tag{6}$$

$$\rho \dot{w} = -\frac{\partial \tilde{p}}{\partial z} + \frac{\partial}{\partial x}\left(\frac{\partial \mathcal{D}}{\partial w_x}\right) + \frac{\partial}{\partial y}\left(\frac{\partial \mathcal{D}}{\partial w_y}\right) + \frac{\partial}{\partial z}\left(\frac{\partial \mathcal{D}}{\partial w_z}\right) \\ - \frac{\partial \mathcal{D}}{\partial \theta}\frac{\partial \theta}{\partial z} - \frac{\partial \mathcal{D}}{\partial \phi}\frac{\partial \phi}{\partial z}, \tag{7}$$

where $\mathcal{D} = \mathcal{D}(\boldsymbol{n}, \boldsymbol{N}, \boldsymbol{A})$ is the nematic viscous dissipation, which depends on the director $\boldsymbol{n}$, the corotational time flux of the director $\boldsymbol{N} = \partial \boldsymbol{n}/\partial t + (\boldsymbol{u} \cdot \nabla)\boldsymbol{n} - (\nabla \boldsymbol{u} - (\nabla \boldsymbol{u})^{\mathrm{T}})\boldsymbol{n}/2$ with $\nabla = \hat{\boldsymbol{x}}\,\partial/\partial x + \hat{\boldsymbol{y}}\,\partial/\partial y + \hat{\boldsymbol{z}}\,\partial/\partial z$, and the rate of the strain tensor $\boldsymbol{A} = (\nabla \boldsymbol{u} + (\nabla \boldsymbol{u})^{\mathrm{T}})/2$ [16]. Also appearing in (5)–(7) are the constant fluid density ρ and the material time derivatives of u, v, and w denoted by $\dot{u}$, $\dot{v}$, and $\dot{w}$, respectively, where, for example, $\dot{u} = \partial u/\partial t + (\boldsymbol{u} \cdot \nabla)u$. Additionally, in (5)–(7), $\tilde{p}$ is the modified pressure [16], henceforth simply called the pressure for brevity, which can be expressed in terms of the fluid pressure p as

$$\tilde{p} = p + W_{\mathrm{F}} - \hat{\Psi}, \tag{8}$$

where $\hat{\Psi} = \hat{\Psi}(x, y, z, t)$ is the bulk energy density corresponding to a general conservative body force [16, Sec. 4.3], for example body forces due to applied electric and/or magnetic fields and gravity, and $W_{\mathrm{F}} = W_{\mathrm{F}}(\boldsymbol{n}, \nabla \boldsymbol{n})$ is the nematic bulk elastic energy density, which depends on the director and spatial derivatives of the director. In what follows, we leave $\hat{\Psi}$ unspecified to keep the approach as general as possible for now, but in Sec. VII, for simplicity, we will neglect any conservative body forces and hence set $\hat{\Psi} \equiv 0$.

Finally, the conservation of angular momentum equations are given by

$$\frac{\partial \mathcal{D}}{\partial \dot{\theta}} = \frac{\partial}{\partial x}\left(\frac{\partial W_{\mathrm{F}}}{\partial \theta_x}\right) + \frac{\partial}{\partial y}\left(\frac{\partial W_{\mathrm{F}}}{\partial \theta_y}\right) + \frac{\partial}{\partial z}\left(\frac{\partial W_{\mathrm{F}}}{\partial \theta_z}\right) \\ - \frac{\partial W_{\mathrm{F}}}{\partial \theta} + \frac{\partial \hat{\Psi}}{\partial \theta}, \tag{9}$$

$$\frac{\partial \mathcal{D}}{\partial \dot{\phi}} = \frac{\partial}{\partial x}\left(\frac{\partial W_{\mathrm{F}}}{\partial \phi_x}\right) + \frac{\partial}{\partial y}\left(\frac{\partial W_{\mathrm{F}}}{\partial \phi_y}\right) + \frac{\partial}{\partial z}\left(\frac{\partial W_{\mathrm{F}}}{\partial \phi_z}\right) \\ - \frac{\partial W_{\mathrm{F}}}{\partial \phi} + \frac{\partial \hat{\Psi}}{\partial \phi}, \tag{10}$$

where $\dot{\theta}$ and $\dot{\phi}$ are the material time derivatives of θ and ϕ. Together, the Ericksen-Leslie equations (4)–(7), (9), and (10) with the unknowns u, v, w, $\tilde{p}$, θ, and ϕ describe the behavior in the bulk of the nematic.

To complete the Ericksen-Leslie equations, we now specify the form of the nematic viscous dissipation $\mathcal{D}$ and the nematic bulk elastic energy density W_{F} appearing in (4)–(7), (9), and (10). In particular, we use of the standard nematic viscous dissipation $\mathcal{D}$ [16], namely

$$\mathcal{D} = \tfrac{1}{2}[\alpha_1(\boldsymbol{n} \cdot \boldsymbol{A}\,\boldsymbol{n})^2 + 2(\alpha_6 - \alpha_5)\boldsymbol{N} \cdot \boldsymbol{A}\,\boldsymbol{n} + \alpha_4 \,\mathrm{tr}(\boldsymbol{A}^2) \\ + (\alpha_5 + \alpha_6)(\boldsymbol{A}\,\boldsymbol{n})^2 + (\alpha_3 - \alpha_2)\boldsymbol{N}^2]. \tag{11}$$

The coefficients $\alpha_1, \ldots, \alpha_6$ appearing in (11) are the Leslie viscosities [16]. The expanded expression for the nematic viscous dissipation $\mathcal{D}$, using the director in the form of (3), the corotational time flux of the director, $\boldsymbol{N}$, and the rate of strain tensor, $\boldsymbol{A}$, is given in Appendix A. For later use, we note that the Leslie viscosities can be expressed in terms of the set of more easily measured nematic viscosities [16], namely the rotational viscosity γ_1, the torsional viscosity γ_2, and the Miesowicz viscosities η_1, η_2, η_3, and η_{12}, as

$$\gamma_1 = \alpha_3 - \alpha_2, \quad \gamma_2 = \alpha_6 - \alpha_5 = \alpha_2 + \alpha_3,$$
$$\eta_1 = \tfrac{1}{2}(\alpha_3 + \alpha_4 + \alpha_6), \quad \eta_2 = \tfrac{1}{2}(-\alpha_2 + \alpha_4 + \alpha_5),$$
$$\eta_3 = \tfrac{1}{2}\alpha_4, \quad \eta_{12} = \alpha_1. \tag{12}$$

We take W_{F} to be the Oseen-Frank bulk elastic energy density, which is defined by

$$W_{\mathrm{F}} = \tfrac{1}{2}K_1(\nabla \cdot \boldsymbol{n})^2 + \tfrac{1}{2}K_2(\boldsymbol{n} \cdot \nabla \times \boldsymbol{n})^2 + \tfrac{1}{2}K_3(\boldsymbol{n} \times \nabla \times \boldsymbol{n})^2 \\ + \tfrac{1}{2}(K_2 + K_4)\nabla \cdot [(\boldsymbol{n} \cdot \nabla)\boldsymbol{n} - (\nabla \cdot \boldsymbol{n})\boldsymbol{n}], \tag{13}$$

where the constants K_1, K_2, and K_3 are the nematic splay, twist and bend elastic constants, respectively, and the combination $K_2 + K_4$ is the saddle-splay elastic constant [16]. To produce a mathematically tractable set of equations, we use the one-constant approximation, and so set $K_1 = K_2 = K_3 = K$ and $K_4 = 0$, where K is the one-constant elastic constant. It is, in principle, possible to proceed without making the one-constant approximation, although the subsequent expressions become considerably more algebraically complicated. In practice, the values of the elastic constants rarely differ by more than a factor of two, and so the one-constant approximation qualitatively describes the behavior [16]. Combining the one-constant approximation, the director in the form of (3), and W_{F} defined by (13), yields the one-constant approximation

of the Oseen–Frank bulk elastic energy W_F [16], given by

$$W_F = \frac{K}{2}[(\nabla\theta)^2 + \cos^2\theta\,(\nabla\phi)^2]. \qquad (14)$$

IV. BOUNDARY CONDITIONS: NEMATIC-PLATE INTERFACES

At the interfaces between the nematic and the lower and upper plates, the boundary conditions for u are standard no-slip and no-penetration conditions, namely

$$u = v = w = 0 \quad \text{on} \quad z = 0 \qquad (15)$$

and

$$u = v = 0 \quad \text{and} \quad w = d' \quad \text{on} \quad z = d. \qquad (16)$$

The boundary conditions on the director at the lower and upper plates are a result of intermolecular forces between the nematic and the material of which the plates are made. These forces can be produced through mechanical and/or chemical treatment of the plates to achieve a variety of desired preferred orientations [51]. For example, photo-curable polymers embedded in the nematic or mechanical rubbing of the plates [52] have been used to create either a homogeneous preferred orientation or a patterned anchoring for which the preferred orientation varies in space. The resulting intermolecular forces lead to an energetically preferred orientation of the director at the nematic-plate interface, which are incorporated into boundary conditions for n, called anchoring conditions.

In situations where the intermolecular forces are strong enough to prescribe the orientation of the director, the anchoring conditions are called infinite anchoring conditions [51]. When the intermolecular forces are weaker than this, the orientation of the director at the plates is also influenced by other effects in the system, such as the torque due to elasticity effects from the bulk of the nematic region. This type of anchoring is known as weak anchoring, and the reorientation of the director away from the preferred orientation is known as anchoring breaking [53].

One particular example of a preferred orientation of the director occurs when the intermolecular forces between the nematic and the plates are such that there is a preferred angle between the director and the plate normal, but the orientation of the director around the plate normal is not fixed. In this scenario the energetic preference is for the director to lie on a cone, a situation known as conical anchoring. Conical anchoring may be infinite, when intermolecular forces are strong enough to prescribe the angle of the director relative to the plate normal, or weak when the orientation of the director at the plates is also influenced by other effects in the system.

In the present work, as particular examples and to simplify the resulting analysis, we use the infinite anchoring conditions discussed above. In particular, we choose two general anchoring conditions that are relevant to a variety of situations. As explained below, we first consider patterned infinite anchoring, which we then specialize to the cases of unidirectional rubbed infinite anchoring with a constant pretilt and axisymmetric patterned infinite anchoring with a constant pretilt. Second, we consider conical infinite anchoring, which we then specialize to the cases of homeotropic infinite anchoring and planar degenerate infinite anchoring.

A. Patterned infinite anchoring

For patterned infinite anchoring, the director has a fixed orientation at each location on each plate, where these directions could, in general, be different on the lower and upper plates. Specifically, patterned infinite anchoring on the lower and upper plates is given by

$$\theta = \Theta_0(x, y) \quad \text{and} \quad \phi = \Phi_0(x, y) \quad \text{on} \quad z = 0 \qquad (17)$$

and

$$\theta = \Theta_d(x, y) \quad \text{and} \quad \phi = \Phi_d(x, y) \quad \text{on} \quad z = d. \qquad (18)$$

In principle, this scenario allows for any patterned design to be considered on each plate—for example, an axisymmetric or periodic pattern—but here we restrict our attention to scenarios where the patterning is the same on both plates, so that

$$\theta = \Theta(x, y) \quad \text{and} \quad \phi = \Phi(x, y) \quad \text{on} \quad z = 0, d, \qquad (19)$$

and consider the following two examples.

1. Unidirectional rubbed infinite anchoring with a constant pretilt

Unidirectional rubbed infinite anchoring may be achieved by coating the surfaces of the plates with a polymeric material and then mechanically rubbing the coating in a particular direction, called the rubbing direction, so that a single preferred director orientation is created [51]. The directional rubbing process creates a preferred twist director angle Φ_c, called the constant rubbing angle. This mechanical rubbing also often creates a preferred tilt director angle, called a pretilt angle, so that the director prefers to align at a fixed angle Θ_c ($0 \leqslant \Theta_c \leqslant \pi/2$) to the normal of the plates. Here we assume that the preferred director orientation is the same on both plates, and so the boundary conditions for the director for unidirectional rubbed infinite anchoring with a constant pretilt on both the lower and upper plates are given by

$$\theta = \Theta_c \quad \text{and} \quad \phi = \Phi_c \quad \text{on} \quad z = 0, d. \qquad (20)$$

2. Axisymmetric patterned infinite anchoring with a constant pretilt

We also consider a case of nonuniform patterning, namely radially independent, axisymmetric patterned infinite anchoring with a constant pretilt. Such nonuniform patterned anchoring may be achieved by optical or mechanical methods, for instance with patterned photoalignment or ion-beam etching [52,54–57], and here we consider the same patterned infinite anchoring with a constant pretilt on both the lower and upper plates, given by

$$\theta = \Theta_c \quad \text{and} \quad \phi = \Phi_c + \tan^{-1}\left(\frac{y}{x}\right) \quad \text{on} \quad z = 0, d. \qquad (21)$$

For the pattern given by (21), Φ_c is the twist angle between the director and the radial vector, and so when $\Phi_c = 0$ the projection of the director field onto the plates is a radial pattern, when $\Phi_c = \pi/2$ the projection of the director field

onto the plates is an azimuthal (i.e., a circular) pattern, and when $0 < \Phi_c < \pi/2$ the projection of the director field onto the plates is a spiral pattern.

B. Conical infinite anchoring

For conical infinite anchoring, the director has a fixed pretilt angle to the plane of the plates, Θ_c, but is free to rotate about the normal of the plates and therefore lies on a cone with constant opening angle $\pi - 2\Theta_c$. In this situation, the boundary condition on the twist director angle is derived from the fact that the torque on the director about the plate normal is zero [16]. For the Oseen-Frank bulk elastic energy (14) this torque condition is $\phi_z = 0$. Conical infinite anchoring on the lower and upper plates is therefore given by

$$\theta = \Theta_c \quad \text{and} \quad \phi_z = 0 \quad \text{on} \quad z = 0, d, \tag{22}$$

and we consider two extreme examples, namely homeotropic infinite anchoring and planar degenerate infinite anchoring.

1. Homeotropic infinite anchoring

The extreme case of conical infinite anchoring when $\Theta_c = \pi/2$, so that the cone opening angle is zero, is termed homeotropic infinite anchoring, and occurs when the director has a preferred orientation perpendicular to the plates. Such anchoring is usually achieved through chemically treating the plates, for instance through coating with a surfactant such as lecithin [51]. When the director is in this preferred orientation we see from (3) that $\mathbf{n} = \hat{\mathbf{z}}$ and the twist director angle ϕ is not defined at the plates. Homeotropic infinite anchoring on the lower and upper plates is then given by

$$\theta = \frac{\pi}{2} \quad \text{and} \quad \phi_z = 0 \quad \text{on} \quad z = 0, d. \tag{23}$$

2. Planar degenerate infinite anchoring

The opposite extreme to homeotropic anchoring occurs when the cone opening angle is $\pi/2$ occurs when $\Theta_c = 0$ and is known as planar degenerate infinite anchoring. In this case the director at each plate is parallel to the plane of the plate but is free to rotate around the normal to the plate. Planar degenerate infinite anchoring on the lower and upper plates is then given by

$$\theta = 0 \quad \text{and} \quad \phi_z = 0 \quad \text{on} \quad z = 0, d. \tag{24}$$

As mentioned above, many other types of anchoring are possible, several of which would lead to interesting situations, for example, weak anchoring conditions [51]. A similar analysis to that described below may be possible, but to keep the resulting analysis analytically tractable, we will not pursue these other forms of anchoring in this work.

V. BOUNDARY CONDITIONS: FREE SURFACE

As we will see in Secs. VI to IX, the depth-averaged governing equations for nematic Hele-Shaw flow are formulated using only the boundary conditions for $\mathbf{u}$ and $\mathbf{n}$ on the lower and upper plates. Boundary conditions for $\mathbf{u}$, $\mathbf{n}$, and p on the free surface $\partial\Omega$ may be subsequently needed in order to tackle specific situations in which, for example, the nematic is surrounded by an ambient gas, an isotropic fluid, a different

nematic material, or a solid boundary. Such boundary conditions on the free surface can be derived through the usual approach of considering balances of mass, stress, and torque [16,51,58]. In the present work, we will not restrict ourselves to specific forms of the free surface boundary conditions in order to keep the approach as general as possible, until Sec. X, in which we consider the flow of nematic according to a simple model for the squeezing stage of the ODF method by prescribing the behavior of the free surface.

We now introduce an appropriate nondimensionalization before deriving the thin-film Ericksen-Leslie equations that govern the flow and director within a nematic Hele-Shaw cell.

VI. NONDIMENSIONALIZATION

We proceed by nondimensionalizing all independent and dependent variables with appropriate scales. We assume that, because of whatever specific situation we are considering, we may define a characteristic length scale of variations in the xy plane, which we denote by L, and a characteristic length scale of variations in the z direction, which we denote by D. Lengths in the xy-plane are therefore nondimensionalized with L, while lengths in the z direction are nondimensionalized with D, and we may define the nondimensional aspect ratio of the Hele-Shaw cell, denoted δ, by

$$\delta = \frac{D}{L}. \tag{25}$$

The characteristic velocity scale in the xy plane is denoted by U, for which there are several equally sensible choices, including $U = GD^2/\mu$ for a flow driven by a constant pressure gradient G; $U = Q/(LD)$ for a flow driven by a prescribed flux Q; and $U = S\sqrt{V/(4\pi D^3)}$ for a flow driven by squeezing a circular cylindrical volume V of nematic between parallel plates with a characteristic plate speed S. In what follows, we leave U unspecified to keep the approach as general as possible for now, but in Sec. X we will use the velocity scale $U = S\sqrt{V/(4\pi D^3)}$. The characteristic timescale is denoted by τ and will also remain unspecified until later in this section, when the possible choices for τ will be described. The conservation of mass equation (4) implies that the velocity scale in the z direction is δU. The pressure is nondimensionalized so that it appears in the leading-order problem. Finally, all viscosities are nondimensionalized using the classical Newtonian viscosity $\mu = \eta_3 = \alpha_4/2$. In summary, the Ericksen-Leslie equations (4)–(7), (9), and (10) are nondimensionalized according to

$$x = L x^*, \quad y = L y^*, \quad z = D z^* = \delta L z^*, \quad t = \tau t^*,$$

$$d = D d^* = \delta L d^*, \quad u = U u^*, \quad v = U v^*, \quad w = \delta U w^*,$$

$$\tilde{p} = \frac{\mu U}{\delta^2 L} \tilde{p}^*, \quad \alpha_1 = \mu \alpha_1^*, \quad \alpha_2 = \mu \alpha_2^*, \quad \alpha_3 = \mu \alpha_3^*,$$

$$\alpha_4 = \mu \alpha_4^*, \quad \alpha_5 = \mu \alpha_5^*, \quad \alpha_6 = \mu \alpha_6^*, \quad \gamma_1 = \mu \gamma_1^*,$$

$$\gamma_2 = \mu \gamma_2^*, \quad \eta_1 = \mu \eta_1^*, \quad \eta_2 = \mu \eta_2^*, \quad \eta_3 = \mu \eta_3^*,$$

$$\eta_{12} = \mu \eta_{12}^*, \tag{26}$$

where the stars denote nondimensional variables. Henceforth, the stars are dropped, and all variables are nondimensional

unless stated otherwise, except for the characteristic velocity scale U and the characteristic timescale τ.

A. Thin-film flow

We now proceed in a similar way to the standard thin-film approach used for isotropic Hele-Shaw flow, based on the assumption that the characteristic length scale of variations in the xy plane is much larger than the characteristic length scale of variations in the z direction, so that the aspect ratio $\delta = D/L$ is small, specifically $\delta \ll 1$.

After applying the nondimensionalization (26), the conservation of mass equation (4) remains the same, and the linear momentum equations (5)–(7) become

$$\frac{\tau_2}{\tau} \frac{\partial u}{\partial t} + \delta \mathrm{Re} \left(u \frac{\partial u}{\partial x} + v \frac{\partial u}{\partial y} + w \frac{\partial u}{\partial z} \right)$$

$$= -\frac{\partial \tilde{p}}{\partial x} + \frac{\partial}{\partial z} \left[g_1(\theta, \phi) \frac{\partial u}{\partial z} + g_3(\theta, \phi) \frac{\partial v}{\partial z} \right]$$

$$+ \frac{\delta \tau_1}{\tau} \frac{\partial}{\partial z} \left[m(\theta) \cos \phi \frac{\partial \theta}{\partial t} + q(\theta) \sin \phi \frac{\partial \phi}{\partial t} \right]$$

$$+ O\left(\delta, \delta^2 \frac{\tau_1}{\tau} \right), \tag{27}$$

$$\frac{\tau_2}{\tau} \frac{\partial v}{\partial t} + \delta \mathrm{Re} \left(u \frac{\partial v}{\partial x} + v \frac{\partial v}{\partial y} + w \frac{\partial v}{\partial z} \right)$$

$$= -\frac{\partial \tilde{p}}{\partial y} + \frac{\partial}{\partial z} \left[g_3(\theta, \phi) \frac{\partial u}{\partial z} + g_2(\theta, \phi) \frac{\partial v}{\partial z} \right]$$

$$+ \frac{\delta \tau_1}{\tau} \frac{\partial}{\partial z} \left[m(\theta) \sin \phi \frac{\partial \theta}{\partial t} - q(\theta) \cos \phi \frac{\partial \phi}{\partial t} \right]$$

$$+ O\left(\delta, \delta^2 \frac{\tau_1}{\tau} \right), \tag{28}$$

$$\frac{\delta^2 \tau_2}{\tau} \frac{\partial w}{\partial t} + \delta^3 \mathrm{Re} \left(u \frac{\partial w}{\partial x} + v \frac{\partial w}{\partial y} + w \frac{\partial w}{\partial z} \right)$$

$$= -\frac{\partial \tilde{p}}{\partial z} + \delta^2 \frac{\tau_1}{\tau} \left[\gamma_2 \frac{\partial}{\partial z} \left(\sin \theta \cos \theta \frac{\partial \theta}{\partial t} \right) \right.$$

$$\left. - \gamma_1 \left(\frac{\partial \theta}{\partial z} \frac{\partial \theta}{\partial t} + \cos^2 \theta \frac{\partial \phi}{\partial t} \frac{\partial \phi}{\partial z} \right) \right]$$

$$+ O\left(\delta, \delta^3 \frac{\tau_1}{\tau} \right), \tag{29}$$

where $g_1(\theta, \phi)$, $g_2(\theta, \phi)$, and $g_3(\theta, \phi)$ are effective viscosity functions defined by

$$g_1(\theta, \phi) = \eta_1 \cos^2 \theta \cos^2 \phi + \eta_2 \sin^2 \theta + \cos^2 \theta \sin^2 \phi$$

$$+ \eta_{12} \sin^2 \theta \cos^2 \theta \cos^2 \phi, \tag{30}$$

$$g_2(\theta, \phi) = \eta_1 \cos^2 \theta \sin^2 \phi + \eta_2 \sin^2 \theta + \cos^2 \theta \cos^2 \phi$$

$$+ \eta_{12} \sin^2 \theta \cos^2 \theta \sin^2 \phi, \tag{31}$$

$$g_3(\theta, \phi) = \eta_1 \cos^2 \theta \sin \phi \cos \phi - \cos^2 \theta \sin \phi \cos \phi$$

$$+ \eta_{12} \sin^2 \theta \cos^2 \theta \sin \phi \cos \phi. \tag{32}$$

Note that the effective viscosity functions $g_1(\theta, \phi)$ and $g_2(\theta, \phi)$ are related through a $\pi/2$ shift in the twist angle ϕ, i.e., $g_1(\theta, \phi) = g_2(\theta, \pi/2 - \phi)$, and that the effective viscosity functions can be related to the standard effective viscosity functions $g(\theta)$ and $h(\theta)$ [16], which are defined by

$$g(\theta) = \eta_1 \cos^2 \theta + \eta_2 \sin^2 \theta + \eta_{12} \sin^2 \theta \cos^2 \theta, \tag{33}$$

$$h(\theta) = \eta_2 \sin^2 \theta + \cos^2 \theta, \tag{34}$$

according to

$$h(\theta) = g_1(\theta, \pi/2) = g_2(\theta, 0), \tag{35}$$

$$g(\theta) = g_1(\theta, 0) = g_2(\theta, \pi/2)$$

$$= g_1(\theta, \phi) + g_3(\theta, \phi) \tan \phi$$

$$= g_2(\theta, \phi) + g_3(\theta, \phi) \cot \phi, \tag{36}$$

$$g(\theta) h(\theta) = g_1(\theta, \phi) g_2(\theta, \phi) - g_3(\theta, \phi)^2. \tag{37}$$

Also appearing in (27)–(29) are two timescales, namely the timescale on which fluid travels the length of the cell, τ_1, which is defined as

$$\tau_1 = \frac{L}{U}, \tag{38}$$

and the fluid inertia timescale τ_2, which is defined in terms of the reduced Reynolds number $\delta \mathrm{Re}$ and τ_1 as

$$\tau_2 = \delta \mathrm{Re} \, \tau_1 = \frac{\rho D^2}{\mu}, \tag{39}$$

where the usual Reynolds number Re, which measures the ratio of inertial effects to viscous effects within the system, is defined by

$$\mathrm{Re} = \frac{\rho U D}{\mu}. \tag{40}$$

As usual, a large Reynolds number therefore corresponds to the situation in which inertial effects are much stronger than viscous effects, while a small Reynolds number corresponds to the opposite situation in which viscous effects are much stronger than inertial effects.

After nondimensionalization, the no-slip and no-penetration conditions (15) and (16) are given by

$$u = v = w = 0 \quad \text{on} \quad z = 0 \tag{41}$$

and

$$u = v = 0 \quad \text{and} \quad w = \frac{\tau_1}{\tau} d' \quad \text{on} \quad z = d. \tag{42}$$

Similarly, applying the nondimensionalization (26) to the angular momentum equations (9) and (10) and collecting terms in orders of δ yields

$$\gamma_1 \frac{\tau_3}{\tau} \frac{\partial \theta}{\partial t}$$

$$= \frac{\partial^2 \theta}{\partial z^2} + \sin \theta \cos \theta \left(\frac{\partial \phi}{\partial z} \right)^2$$

$$+ \delta^2 \left[\frac{\partial^2 \theta}{\partial x^2} + \frac{\partial^2 \theta}{\partial y^2} + \sin \theta \cos \theta \left(\left(\frac{\partial \phi}{\partial x} \right)^2 + \left(\frac{\partial \phi}{\partial y} \right)^2 \right) \right]$$

$$- \operatorname{Er} m(\theta) \left(\cos \phi \, \frac{\partial u}{\partial z} + \sin \phi \, \frac{\partial v}{\partial z} \right)$$

$$+ \frac{\delta^2 L^2}{K} \frac{\partial \hat{\Psi}}{\partial \theta} + O(\delta \operatorname{Er}), \tag{43}$$

and

$$\gamma_1 \frac{\tau_3}{\tau} \cos^2 \theta \, \frac{\partial \phi}{\partial t}$$

$$= \frac{\partial}{\partial z} \left(\cos^2 \theta \, \frac{\partial \phi}{\partial z} \right)$$

$$+ \delta^2 \left[\frac{\partial}{\partial x} \left(\cos^2 \theta \, \frac{\partial \phi}{\partial x} \right) + \frac{\partial}{\partial y} \left(\cos^2 \theta \, \frac{\partial \phi}{\partial y} \right) \right]$$

$$- \operatorname{Er} q(\theta) \left(\sin \phi \, \frac{\partial u}{\partial z} - \cos \phi \, \frac{\partial v}{\partial z} \right)$$

$$+ \frac{\delta^2 L^2}{K} \frac{\partial \hat{\Psi}}{\partial \phi} + O(\delta \operatorname{Er}), \tag{44}$$

where Er is the Ericksen number, defined by

$$\operatorname{Er} = \frac{\mu D U}{K}, \tag{45}$$

a measure of the ratio of viscous effects to elasticity effects within the system. A large Ericksen number therefore corresponds to the situation in which viscous effects are much stronger than elasticity effects, while a small Ericksen number corresponds to the opposite situation in which elasticity effects are much stronger than viscous effects. Also appearing in (43) and (44) is a third timescale, the director rotation timescale τ_3, which is defined as

$$\tau_3 = \frac{\mu D^2}{K}. \tag{46}$$

Additionally, the functions $m(\theta)$ and $q(\theta)$ appearing in (43) and (44) are effective viscosity functions, which are defined by

$$m(\theta) = \tfrac{1}{2} \left(\gamma_1 + \gamma_2 \cos 2\theta \right)$$

$$\text{and} \quad q(\theta) = \tfrac{1}{2} \left(\gamma_1 - \gamma_2 \right) \sin \theta \cos \theta. \tag{47}$$

The anchoring conditions on the plates discussed in Sec. IV, are unchanged after applying the nondimensionalization (26).

Note that in (27)–(29), (43), and (44) we have retained the terms with coefficients of τ_1/τ, τ_2/τ, and τ_3/τ that are the lowest order in δ as the choice of the timescale τ discussed subsequently may change the order in δ at which these terms appear.

B. Characteristic timescales

Inspection of the nondimensional Ericksen-Leslie equations (4), (27)–(29), (43), and (44) shows that there are three natural choices for the timescale τ. In situations in which time-dependent changes in the director angles are important, it would be appropriate to nondimensionalize time with the director rotation timescale τ_3, so that $\tau = \tau_3$. This choice of timescale may be appropriate, for instance, when modeling the director rotation due to flow within a channel for which the plates exhibit homeotropic anchoring [30] (for one-dimensional models of these transitions, see [38] and [39]). In

situations in which the dynamics of the flow across the length scale L are of interest, it would be natural to use the timescale $\tau = \tau_1$. On the other hand, when dynamics induced by inertial effects are of particular interest, the choice of timescale $\tau = \tau_2$ is appropriate. Table I shows typical values for the timescales τ_1, τ_2, and τ_3 and the nondimensional numbers δ, Re, and Er for four different situations, namely analysis of the ODF method by Cousins *et al.* [49], capillary-filling experiments by Mi and Yang [15], viscous fingering experiments by Sonin and Bartolino [21], and nematic microfluidic experiments by Sengupta *et al.* [34]. Table I shows that, in all but one extreme case, $\tau_1 \gg \tau_2, \tau_3$. This regime is typical of many situations of relevance to LCD manufacturing [49,50], viscous fingering experiments [21,22,24,26], and some experiments with nematic microfluidic channels [28–30].

Given the many applications for which flow over the length scale in the xy plane is relevant, e.g., the cases mentioned above for LCD manufacturing, viscous fingering experiments, and nematic microfluidic experiments, in the present work we choose the timescale to be τ_1. Of course, other situations may require a different choice of timescale, or even more sophisticated analyses involving more than one timescale. Specifically, we set $\tau = \tau_1$ and therefore

$$\frac{\tau_1}{\tau} = 1, \quad \frac{\tau_2}{\tau} = \delta \operatorname{Re}, \quad \text{and} \quad \frac{\tau_3}{\tau} = \delta \operatorname{Er}. \tag{48}$$

Additionally, we assume that viscous effects are much stronger than inertial effects, and hence we assume that the reduced Reynolds number $\delta \operatorname{Re}$ is small, such that $\delta \operatorname{Re} \ll 1$. This is certainly the case for examples given in Table I, where $\delta \operatorname{Re} \approx 10^{-7}$–$10^{-9}$. Also, as mentioned previously, we neglect any conservative body forces and hence set $\hat{\Psi} \equiv 0$.

VII. THIN-FILM ERICKSEN-LESLIE EQUATIONS

We now proceed by employing the standard thin-film approach used for isotropic Hele-Shaw flow and consider only the leading-order problem in the limit $\delta \to 0$. In this limit, and setting $\tau = \tau_1$, $\delta \operatorname{Re} \ll 1$ and $\hat{\Psi} \equiv 0$ in (4), (27)–(29), (43), and (44), as discussed above, the leading-order Ericksen-Leslie equations, hereafter referred to as the thin-film Ericksen-Leslie equations, are given by

$$0 = \frac{\partial u}{\partial x} + \frac{\partial v}{\partial y} + \frac{\partial w}{\partial z}, \tag{49}$$

$$\frac{\partial \tilde{p}}{\partial x} = \frac{\partial}{\partial z} \left[g_1(\theta, \phi) \frac{\partial u}{\partial z} + g_3(\theta, \phi) \frac{\partial v}{\partial z} \right], \tag{50}$$

$$\frac{\partial \tilde{p}}{\partial y} = \frac{\partial}{\partial z} \left[g_3(\theta, \phi) \frac{\partial u}{\partial z} + g_2(\theta, \phi) \frac{\partial v}{\partial z} \right], \tag{51}$$

$$\frac{\partial \tilde{p}}{\partial z} = 0, \tag{52}$$

$$0 = \frac{\partial^2 \theta}{\partial z^2} + \sin \theta \cos \theta \left(\frac{\partial \phi}{\partial z} \right)^2$$

$$- \operatorname{Er} m(\theta) \left(\cos \phi \, \frac{\partial u}{\partial z} + \sin \phi \, \frac{\partial v}{\partial z} \right), \tag{53}$$

TABLE I. Typical values for the timescales τ_1, τ_2, and τ_3 and the nondimensional numbers δ, Re, and Er for four different situations, namely analysis of the ODF method by Cousins *et al.* [47,49], capillary-filling experiments by Mi and Yang [15], viscous fingering experiments by Sonin and Bartolino [21], and nematic microfluidic experiments by Sengupta *et al.* [34]. A full statement of all of the parameter values used to generate these values is given in Appendix B.

		τ_1 (s)	τ_2 (s)	τ_3 (s)	δ	Re	Er
Analysis of the ODF method	min.	5.0×10^{-2}	2.5×10^{-8}	2.5×10^{-4}		1.0×10^{-5}	1.0×10^{-1}
by Cousins *et al.* [49]	max.	2.5×10^{-1}	2.5×10^{-4}	2.5	1.0×10^{-2}	5.0×10^{-1}	5.0×10^{3}
Capillary-filling experiments							
by Mi and Yang [15]		1.0×10^{3}	3.1×10^{-6}	4.5×10^{-1}	1.0×10^{-4}	3.0×10^{-5}	4.5
Viscous fingering experiments							
by Sonin and Bartolino [21]		1.2×10^{-2}	3.8×10^{-7}	5.5×10^{-2}	3.5×10^{-2}	8.8×10^{-4}	1.3×10^{2}
Nematic microfluidic experiments	min.	3.0×10^{1}	7.8×10^{-5}	2.9×10^{-1}	4.0×10^{-4}	5.0×10^{-5}	7.2
by Sengupta *et al.* [34]	max.	1.0×10^{2}	2.0×10^{-6}	1.1×10^{1}	2.5×10^{-3}	1.0×10^{-3}	1.5×10^{2}

$$0 = \frac{\partial}{\partial z}\left[\cos^2\theta \frac{\partial\phi}{\partial z}\right]$$

$$- \, \mathrm{Er}\, q(\theta)\left(\sin\phi \, \frac{\partial u}{\partial z} - \cos\phi \, \frac{\partial v}{\partial z}\right). \qquad (54)$$

Although (50)–(54) do not include any time derivatives, we note that their solutions can still depend on time t in situations in which the boundary conditions on the plates and/or the free surface are time dependent.

Equation (52) shows that the pressure is independent of z, and hence $\tilde{p} = \tilde{p}(x, y, t)$, but solving the remaining thin-film Ericksen-Leslie equations (50)–(54) is, in general, difficult and may require a numerical approach. In the present work, we take an alternative approach and analyze the thin-film Ericksen-Leslie equations in a number of limiting cases in which we can make significant analytical progress. First, in Sec. VIII, we consider the leading-order problem in the limiting case in which elasticity effects are much stronger than viscous effects, and hence the Ericksen number is small (Er $\ll$ 1). Examples of such situations include the capillary-filling method where flow is driven by capillary action [15] and flows driven by gravity [59]. Second, in Sec. IX, we consider the leading-order problem in the limiting case in which viscous effects are much stronger than elastic effects, and hence the Ericksen number is large (Er $\gg$ 1). Examples of such situations include the ODF method where flow is driven by squeezing [49,50] and in recent experiments using nematic microfluidic devices [30,32,35,60] in which the flow is driven by a large pressure gradient. Finally, we note that, in choosing the Ericksen-Leslie theory to model this system, we are not allowing for the presence of defects within the nematic. Defects are localised regions of high gradients in the director field, with a corresponding reduction in nematic orientational order. Such defects can occur at low Ericksen numbers, for instance in physical systems with complex geometries where solid boundaries and/or free boundaries have opposing anchoring conditions [61], or at high Ericksen numbers, for instance in systems where flow induces high director gradient, and defect elongation along the direction of the flow can occur [62]. In order to model such systems, a theory that allows for changes in the orientational order parameter is required [63], and, while beyond the scope of the present work, a thin-film

analysis of Hele-Shaw flow using this type of model would be an interesting future direction of research.

VIII. THE LIMIT OF SMALL ERICKSEN NUMBER (Er $\ll$ 1)

In this section, we consider the leading-order problem in the limit of small Ericksen number (Er $\ll$ 1), with all the scenarios of anchoring mentioned in Sec. IV. We consider the general case of patterned infinite anchoring in Sec. VIII A, with particular cases of unidirectional rubbed infinite anchoring with a constant pretilt and axisymmetric patterned infinite anchoring with a constant pretilt, and then consider the general case of conical infinite anchoring in Sec. VIII B, with particular cases of homeotropic infinite anchoring and planar degenerate infinite anchoring.

A. Patterned infinite anchoring

We begin by considering the scenario of patterned infinite anchoring, which corresponds to the anchoring conditions (19). At leading order in Er $\ll$ 1, the thin-film conservation of angular momentum equations (53) and (54) subject to (19) are satisfied by the director angle solutions

$$\theta = \Theta(x, y) \quad \text{and} \quad \phi = \Phi(x, y). \qquad (55)$$

Therefore, in this limit, the director field throughout the cell is identical to the director field patterned on the plates. We note that, in the scenario where the patterned infinite anchoring on the two plates is different, a numerical approach is, in general, required to solve for the leading-order director angles θ and ϕ.

At leading order in Er $\ll$ 1, the thin-film conservation of linear momentum equations (50) and (51) are given by

$$\frac{\partial\tilde{p}}{\partial x} = g_1 \frac{\partial^2 u}{\partial z^2} + g_3 \frac{\partial^2 v}{\partial z^2} \quad \text{and} \quad \frac{\partial\tilde{p}}{\partial y} = g_3 \frac{\partial^2 u}{\partial z^2} + g_2 \frac{\partial^2 v}{\partial z^2}, \qquad (56)$$

where $g_1 = g_1(\Phi(x, y), \Theta(x, y))$, $g_2 = g_2(\Phi(x, y), \Theta(x, y))$ and $g_3 = g_3(\Phi(x, y), \Theta(x, y))$. Integrating (56) with respect to z twice, applying the no-slip conditions (41) and (42), and

rearranging yields solutions for u and v,

$$u = \frac{1}{2g\hbar}\left(g_2\frac{\partial\tilde{p}}{\partial x} - g_3\frac{\partial\tilde{p}}{\partial y}\right)z(z-d)$$

$$\text{and} \quad v = \frac{1}{2g\hbar}\left(g_1\frac{\partial\tilde{p}}{\partial y} - g_3\frac{\partial\tilde{p}}{\partial x}\right)z(z-d), \quad (57)$$

where $g = g(\Theta(x,y))$ and $\hbar = h(\Theta(x,y))$. The patterned anchoring, therefore, creates a fixed director field which in turn produces an anisotropic patterned viscosity via the effective viscosity functions g, $\hbar$, g_1, g_2, and g_3. The flow is then driven by the pressure gradients $\partial\tilde{p}/\partial x$ and $\partial\tilde{p}/\partial y$ and differs from the simple isotropic situation due to the patterned viscosity. The streamlines of the flow may therefore be tailored by using plates on which patterned anchoring has been created. This tailoring of the streamlines is an example of the flow being guided by the director field, a situation that has previously been investigated theoretically by Leslie [64], albeit only for a unidirectional director field. However, in this analysis, the fixed director was induced by a strong magnetic field and not by anchoring.

Following the standard approach used in the analysis of Hele-Shaw flow, we now substitute the solutions for the velocity (57) into the conservation of mass equation (49), integrate with respect to z between $z = 0$ and $z = d$, and apply the no-slip and no-penetration conditions (41) and (42), to give the governing equation for the pressure $\tilde{p}$, namely

$$\frac{\partial}{\partial x}\left[\frac{1}{g\hbar}\left(g_2\frac{\partial\tilde{p}}{\partial x} - g_3\frac{\partial\tilde{p}}{\partial y}\right)\right] + \frac{\partial}{\partial y}\left[\frac{1}{g\hbar}\left(g_1\frac{\partial\tilde{p}}{\partial y} - g_3\frac{\partial\tilde{p}}{\partial x}\right)\right]$$
$$= \frac{12d'}{d^3}. \quad (58)$$

Finally, we repeat this process by substituting the solutions for the velocity (57) into the conservation of mass equation (49), but now integrating with respect to z between $z = 0$ and z, applying the no-slip condition (41), and simplifying the expression by substituting (58) to give the vertical velocity,

$$w = \frac{d'}{d^3}(3d - 2z)z^2, \quad (59)$$

which is independent of the director angles and identically zero when the upper plate is stationary. After $\tilde{p}$ has been obtained from (58), the velocity components u and v can be calculated from (57). In general, for a nonhomogeneous anchoring pattern, the solution for $\tilde{p}$ from (58) must be obtained numerically; however, as we shall see shortly, there are cases in which the symmetry of the anchoring pattern allows for further analytical progress.

In summary, in the scenario of patterned infinite anchoring, the thin-film Ericksen-Leslie equations (50)–(54) can be written in terms of the unknown pressure $\tilde{p}$ as

$$u = \frac{1}{2g\hbar}\left(g_2\frac{\partial\tilde{p}}{\partial x} - g_3\frac{\partial\tilde{p}}{\partial y}\right)z(z-d),$$

$$v = \frac{1}{2g\hbar}\left(g_1\frac{\partial\tilde{p}}{\partial y} - g_3\frac{\partial\tilde{p}}{\partial x}\right)z(z-d),$$

$$w = \frac{d'}{d^3}(3d - 2z)z^2,$$

$$\frac{\partial}{\partial x}\left[\frac{1}{g\hbar}\left(g_2\frac{\partial\tilde{p}}{\partial x} - g_3\frac{\partial\tilde{p}}{\partial y}\right)\right] + \frac{\partial}{\partial y}\left[\frac{1}{g\hbar}\left(g_1\frac{\partial\tilde{p}}{\partial y} - g_3\frac{\partial\tilde{p}}{\partial x}\right)\right]$$
$$= \frac{12d'}{d^3},$$

$$\theta \equiv \Theta(x,y), \quad \phi = \Phi(x,y). \quad (60)$$

We now consider the particular cases of unidirectional rubbed infinite anchoring with a constant pretilt and axisymmetric patterned infinite anchoring with a constant pretilt.

1. Unidirectional rubbed infinite anchoring with a constant pretilt

For unidirectional rubbed infinite anchoring with a constant pretilt, namely (19) with (20), the solution to (60) may be obtained using a rotation of the xy coordinate system to a new $\hat{x}\hat{y}$ coordinate system in which the projection of the preferred director at the plates is a coordinate axis,

$$\hat{x} = \frac{1}{\sqrt{h_c}}(\cos\Phi_c\, x + \sin\Phi_c\, y),$$

$$\hat{y} = \frac{1}{\sqrt{g_c}}(-\sin\Phi_c\, x + \cos\Phi_c\, y), \quad (61)$$

where $h_c = h(\Theta_c)$ and $g_c = g(\Theta_c)$. At leading order in $\mathrm{Er} \ll 1$, the thin-film Ericksen-Leslie equations (50)–(54) can then be written in terms of the unknown pressure $\tilde{p}$ as

$$\hat{u} = \frac{1}{2g_c}\frac{\partial\tilde{p}}{\partial\hat{x}}z(z-d),$$

$$\hat{v} = \frac{1}{2h_c}\frac{\partial\tilde{p}}{\partial\hat{y}}z(z-d),$$

$$w = \frac{d'}{d^3}(3d - 2z)z^2,$$

$$\frac{\partial^2\tilde{p}}{\partial\hat{x}^2} + \frac{\partial^2\tilde{p}}{\partial\hat{y}^2} = \frac{12h_c g_c d'}{d^3},$$

$$\theta \equiv \Theta_c, \quad \phi \equiv \Phi_c. \quad (62)$$

In (62), $\hat{u}$ and $\hat{v}$ are the velocity components parallel and perpendicular to the rubbing direction, respectively. Note that $\hat{u}$ and $\hat{v}$ given by (62) can be reformulated in terms of the gradient of the pressure in the original Cartesian coordinates as

$$\hat{u} = \sqrt{\frac{h_c}{4g_c^2}}\left(\cos\Phi_c\frac{\partial\tilde{p}}{\partial x} + \sin\Phi_c\frac{\partial\tilde{p}}{\partial y}\right)z(z-d)$$

$$\text{and} \quad \hat{v} = \sqrt{\frac{g_c}{4h_c^2}}\left(-\sin\Phi_c\frac{\partial\tilde{p}}{\partial x} + \cos\Phi_c\frac{\partial\tilde{p}}{\partial y}\right)z(z-d). \quad (63)$$

For instance, a constant pressure gradient applied in the x direction, i.e., when $G = \partial\tilde{p}/\partial x$ and $\partial\tilde{p}/\partial y = 0$, leads to a flow given by

$$\hat{u} = \sqrt{\frac{h_c}{4g_c^2}}\cos\Phi_c\, Gz(z-d)$$

$$\text{and} \quad \hat{v} = -\sqrt{\frac{g_c}{4h_c^2}}\sin\Phi_c\, Gz(z-d). \quad (64)$$

The solutions in (64) show that the flow is driven by the pressure gradient in the x direction but guided by the

patterned viscosity that has been induced by the rubbed anchoring. In particular, (64) shows that the magnitude of the velocity component parallel to the rubbing direction $|\hat{u}|$ is greater than the magnitude of the velocity component perpendicular to the rubbing direction $|\hat{v}|$ provided that $\tan \Phi_c < (h_c/g_c)^{3/2}$. So, for example, for unidirectional rubbed anchoring with $\Theta_c = 0$ and $\Phi_c = \pi/4$, and for the nematic $4'$-pentyl-4-biphenylcarbonitrile (5CB) [65], which has dimensional viscosity values $\eta_1 = 0.0204$ Pa s and $\eta_3 = 0.0326$ Pa s, and therefore nondimensional viscosity value $\eta_1^* = \eta_1/\eta_3 = 0.626$, we have $\tan \Phi_c = 1$ and $(h_c/g_c)^{3/2} = (1/\eta_1^*)^{3/2} = 2.02$, and hence $|\hat{u}|/|\hat{v}| = 2.02$ and the flow is predominately in the rubbing direction.

2. Axisymmetric infinite anchoring with a constant pretilt

For axisymmetric infinite anchoring with a constant pretilt, namely (19) with (21), we use the polar coordinate transform,

$$x = r\cos(\beta - \Phi_c), \quad y = r\sin(\beta - \Phi_c) \tag{65}$$

in (60), where r and β are the usual radial and azimuthal coordinates, respectively, and at leading order in Er $\ll 1$ the thin-film Ericksen-Leslie equations (50)–(54) can be written in terms of the unknown pressure $\tilde{p}$ as

$$u_r = \frac{1}{2g_c h_c}\left(g_{2c}\frac{\partial \tilde{p}}{\partial r} + 2g_{3c}\frac{1}{r}\frac{\partial \tilde{p}}{\partial \beta}\right)z(z-d),$$

$$u_\beta = \frac{1}{2g_c h_c}\left(g_{1c}\frac{1}{r}\frac{\partial \tilde{p}}{\partial \beta} + 2g_{3c}\frac{\partial \tilde{p}}{\partial r}\right)z(z-d),$$

$$w = \frac{d'}{d^3}(3d - 2z)z^2,$$

$$g_{1c}\frac{1}{r^2}\frac{\partial^2 \tilde{p}}{\partial \beta^2} + 2g_{3c}\frac{1}{r}\frac{\partial \tilde{p}}{\partial \beta}r + g_{2c}\frac{1}{r}\frac{\partial}{\partial r}\left(r\frac{\partial \tilde{p}}{\partial r}\right)$$

$$= \frac{12h_c g_c d'}{d^3},$$

$$\theta \equiv \Theta_c, \quad \phi = \Phi_c + \beta, \tag{66}$$

where $g_{1c} = g_1(\Theta_c, \Phi_c)$, $g_{2c} = g_2(\Theta_c, \Phi_c)$, and $g_{3c} = g_3(\Theta_c, \Phi_c)$.

Inspection of (32) and (66) shows that in situations in which the anchoring pattern is strictly radial or strictly azimuthal, i.e., when $\Phi_c = 0$ or $\Phi_c = \pi/2$, then $g_{3c} \equiv 0$ and there is a radial-flow solution that satisfies (66) for which $\partial \tilde{p}/\partial \beta = 0$ and hence $u_\beta \equiv 0$. In these situations, $\tilde{p}$ can be obtained by direct integration of the pressure equation in (66) subject to appropriate boundary conditions on $\partial \Omega$. Conversely, in situations in which the anchoring pattern is not strictly radial or strictly azimuthal, i.e., when $\Phi_c \neq 0$ or $\Phi_c \neq \pi/2$, then $g_{3c} \neq 0$ and no purely radial-flow solution satisfies (66), and the flow is a spiral, guided by the axisymmetric anchoring pattern.

B. Conical infinite anchoring

For conical infinite anchoring, which corresponds to the anchoring conditions (22), at leading order in Er $\ll 1$, the

thin-film conservation of angular momentum equations (53) and (54) are satisfied by the director angle solutions

$$\theta \equiv \Theta_c \quad \text{and} \quad \phi = \phi(x, y, t). \tag{67}$$

To determine ϕ we must consider higher-order thin-film conservation of angular momentum equations [specifically, (43) and (44) at first order in δ^2]. Provided that Er $\ll \delta^2 \ll 1$, we find that the equations yield that the twist director angle ϕ is governed by Laplace's equation, namely

$$\frac{\partial^2 \phi}{\partial x^2} + \frac{\partial^2 \phi}{\partial y^2} = 0, \tag{68}$$

subject to appropriate boundary conditions on $\partial \Omega$. Note that unlike in the scenario of patterned anchoring, previously discussed in Sec. VIII A, in which the anchoring on the plates fixes the director field throughout the cell, in the scenario of conical anchoring, the director field is determined by the anchoring on both the plates and $\partial \Omega$.

At leading order in Er $\ll 1$, the thin-film Ericksen–Leslie equations (50)–(54) can therefore be written in terms of the unknown pressure $\tilde{p}$ and twist angle ϕ as

$$u = \frac{1}{2h_c g_c}\left(g_2\frac{\partial \tilde{p}}{\partial x} - g_3\frac{\partial \tilde{p}}{\partial y}\right)z(z-d),$$

$$v = \frac{1}{2h_c g_c}\left(g_1\frac{\partial \tilde{p}}{\partial y} - g_3\frac{\partial \tilde{p}}{\partial x}\right)z(z-d),$$

$$w = \frac{d'}{d^3}(3d - 2z)z^2,$$

$$\frac{\partial}{\partial x}\left(g_2\frac{\partial \tilde{p}}{\partial x} - g_3\frac{\partial \tilde{p}}{\partial y}\right) + \frac{\partial}{\partial y}\left(g_1\frac{\partial \tilde{p}}{\partial y} - g_3\frac{\partial \tilde{p}}{\partial x}\right)$$

$$= \frac{12h_c g_c d'}{d^3},$$

$$\theta \equiv \Theta_c, \quad \frac{\partial^2 \phi}{\partial x^2} + \frac{\partial^2 \phi}{\partial y^2} = 0. \tag{69}$$

We now consider the particular cases of homeotropic infinite anchoring and planar degenerate infinite anchoring.

1. Homeotropic infinite anchoring

For homeotropic infinite anchoring, which corresponds to the anchoring conditions (19) with $\Theta = \pi/2$, at leading order in Er $\ll 1$ the thin-film Ericksen-Leslie equations (50)–(54) can be written in terms of the unknown pressure $\tilde{p}$ as

$$u = \frac{1}{2\eta_2}\frac{\partial \tilde{p}}{\partial x}z(z-d),$$

$$v = \frac{1}{2\eta_2}\frac{\partial \tilde{p}}{\partial y}z(z-d),$$

$$w = \frac{d'}{d^3}(3d - 2z)z^2,$$

$$\frac{\partial^2 \tilde{p}}{\partial x^2} + \frac{\partial^2 \tilde{p}}{\partial y^2} = \frac{12\eta_2 d'}{d^3}, \quad \theta \equiv \frac{\pi}{2}, \tag{70}$$

and we note that with $\theta \equiv \pi/2$ the twist director angle ϕ is not defined. In this situation, the director is therefore fixed perpendicular to the xy plane, i.e., $\boldsymbol{n} = \hat{\boldsymbol{z}}$, throughout the cell (a situation sometimes called uniform homeotropic orientation).

TABLE II. A summary of the thin-film Ericksen-Leslie equations (50)–(54) in the limit of small Ericksen number (Er $\ll$ 1) in terms of the unknown pressure $\tilde{p}$ (and the unknown twist angle ϕ in the scenario of conical infinite anchoring). Expressions for the tilt director angle θ, the twist director angle ϕ, the pressure $\tilde{p}$, and the velocities u, v, and w are stated. The transformed coordinates $\hat{x}$, $\hat{y}$, r, and β are defined by (61) and (65).

	Small Ericksen number Er $\ll$ 1					
	Patterned infinite anchoring (Sec. VIII A)			Conical infinite anchoring (Sec. VIII B)		
	General	Rubbed	Axisymmetric	General	Homeotropic	Planar degenerate
θ	$\Theta(x,y)$		Θ_c		$\dfrac{\pi}{2}$	0
ϕ	$\Phi(x,y)$	Φ_c	$\Phi_c + \beta$	$\dfrac{\partial^2 \phi}{\partial x^2} + \dfrac{\partial^2 \phi}{\partial y^2} = 0$	undefined	$\dfrac{\partial^2 \phi}{\partial x^2} + \dfrac{\partial^2 \phi}{\partial y^2} = 0$
$\tilde{p}$	(58)	$\dfrac{\partial^2 \tilde{p}}{\partial \hat{x}^2} + \dfrac{\partial^2 \tilde{p}}{\partial \hat{y}^2} = \dfrac{12 h_c g_c d'}{d^3}$	(66)	(69)	$\dfrac{\partial^2 \tilde{p}}{\partial x^2} + \dfrac{\partial^2 \tilde{p}}{\partial y^2} = \dfrac{12 \eta_2 d'}{d^3}$	(71)
u	(57)	$\hat{u} = \dfrac{1}{2g_c}\dfrac{\partial \tilde{p}}{\partial \hat{x}} z(z-d)$	(66)	(69)	$u = \dfrac{1}{2\eta_2}\dfrac{\partial \tilde{p}}{\partial x}(z-d)z$	(71)
v	(57)	$\hat{v} = \dfrac{1}{2h_c}\dfrac{\partial \tilde{p}}{\partial \hat{y}} z(z-d)$	(66)	(69)	$v = \dfrac{1}{2\eta_2}\dfrac{\partial \tilde{p}}{\partial y}(z-d)z$	(71)
w			$\dfrac{d'}{d^3}(3d-2z)z^2$			

The governing equation for the pressure, given in (70), takes the same form as for isotropic Hele-Shaw flow, and therefore the flow of a nematic with homeotropic infinite anchoring is identical to that of the flow of an isotropic fluid with viscosity η_2.

2. Planar degenerate infinite anchoring

For the degenerate form of conical infinite anchoring called planar degenerate infinite anchoring, which corresponds to the anchoring conditions (22) with $\Theta_c = 0$, the thin-film Ericksen-Leslie equations (50)–(54) can be written in terms of the unknown pressure $\tilde{p}$ as

$$u = \frac{1}{2\eta_1}\left(\hbar_2 \frac{\partial \tilde{p}}{\partial x} - \hbar_3 \frac{\partial \tilde{p}}{\partial y}\right)z(z-d),$$

$$v = \frac{1}{2\eta_1}\left(\hbar_1 \frac{\partial \tilde{p}}{\partial y} - \hbar_3 \frac{\partial \tilde{p}}{\partial x}\right)z(z-d),$$

$$w = \frac{d'}{d^3}(3d-2z)z^2,$$

$$\frac{\partial}{\partial x}\left(\hbar_2 \frac{\partial \tilde{p}}{\partial x} - \hbar_3 \frac{\partial \tilde{p}}{\partial y}\right) + \frac{\partial}{\partial y}\left(\hbar_1 \frac{\partial \tilde{p}}{\partial y} - \hbar_3 \frac{\partial \tilde{p}}{\partial x}\right) = \frac{12\eta_1 d'}{d^3},$$

$$\theta \equiv 0, \quad \frac{\partial^2 \phi}{\partial x^2} + \frac{\partial^2 \phi}{\partial y^2} = 0, \qquad (71)$$

where $\hbar_1(\phi) = g_1(0,\phi) = \eta_1 \cos^2\phi + \sin^2\phi$, $\hbar_2(\phi) = g_2(0,\phi) = \eta_1 \sin^2\phi + \cos^2\phi$, and $\hbar_3(\phi) = g_3(0,\phi) = \eta_1 \sin\phi\cos\phi - \sin\phi\cos\phi$. In general, the solution of this set of equations is found by first solving the Laplace equation for ϕ subject to a boundary condition on $\partial\Omega$, then substituting the solution for ϕ into the differential equation for $\tilde{p}$ and solving for $\tilde{p}$ subject to an appropriate boundary condition on $\partial\Omega$.

Table II summarizes the scenarios we have considered in the limit of small Ericksen number (Er $\ll$ 1).

IX. THE LIMIT OF LARGE ERICKSEN NUMBER (Er $\gg$ 1)

In the limit of large Ericksen number (Er $\gg$ 1), viscous effects are much stronger than elasticity effects and there are two distinct cases to consider, namely when the nematic is a flow-aligning nematic or a non-flow-aligning nematic. These two cases, which we consider in Secs. IX A and IX B, respectively, arise at leading order in Er $\gg$ 1 from the thin-film angular momentum equations (53) and (54), which are satisfied by either

$$m(\theta) = 0 \quad \text{and} \quad \sin\phi\,\frac{\partial u}{\partial z} - \cos\phi\,\frac{\partial v}{\partial z} = 0 \qquad (72)$$

or

$$q(\theta) = 0 \quad \text{and} \quad \cos\phi\,\frac{\partial u}{\partial z} + \sin\phi\,\frac{\partial v}{\partial z} = 0. \qquad (73)$$

From the definitions of $m(\theta)$ and $q(\theta)$ in (47) it is clear that, for general values of the viscosity parameters γ_1 and γ_2, solutions satisfying (72) or (73) are mutually exclusive. Also, we see from the definition of $m(\theta)$ in (47) that a solution satisfying (72) is only possible when $-\gamma_2 > \gamma_1$. A material that obeys this condition is known as a flow-aligning nematic [16]. When a solution satisfying (72) is not possible, i.e., when $\gamma_1 > -\gamma_2$, the nematic material is known as a non-flow-aligning nematic or a tumbling nematic [16], and so a solution satisfying (73) is then required. We note that solutions to (72) or (73) do not satisfy the anchoring conditions discussed in Sec. IV, the anchoring being broken by the flow effects; however, these leading order in Er $\gg$ 1 equations provide the leading-order solutions away from the boundaries of the region and the boundary conditions will be satisfied via appropriate boundary layers [39,50], as discussed in the next section.

A. Flow-aligning nematics

For a flow-aligning nematic, the definition of $m(\theta)$ given in (47) yields the well-known flow-alignment solution, $\theta \equiv \pm\theta_L$,

where

$$\theta_L = \frac{1}{2}\cos^{-1}\left(-\frac{\gamma_1}{\gamma_2}\right) \qquad (74)$$

is the Leslie or flow-alignment angle [16]. A stability analysis of the full system (27)–(29), (43), and (44) previously showed that in regions of positive or negative shear rate the director angle prefers to align at the positive Leslie angle θ_L or the negative Leslie angle $-\theta_L$, respectively, [16]. As also previously demonstrated [38,39,50], this solution is an outer solution (i.e., a solution in the bulk of the cell away from the plates and away from any internal location of director reorientation) and the solution for θ has boundary layers of thickness $O(\mathrm{Er}^{-1/2}) \ll 1$ near to the plates, in which the director adjusts to satisfy the anchoring conditions at the plates, and an internal layer of thickness $O(\mathrm{Er}^{-1/3}) \ll 1$ near the center of the cell, which separates the regions of positive and negative shear rate and positive Leslie angle θ_L and negative Leslie angle $-\theta_L$, respectively. In the present work, we use this outer solution and assume that the internal layer (and therefore the change in the sign of shear rate) is located at $z = d/2$. Hence, at leading-order in $\mathrm{Er} \gg 1$, the solution for θ is given by

$$\theta = \begin{cases} +\theta_L & \text{when} \quad 0 \leqslant z \leqslant d/2, \\ -\theta_L & \text{when} \quad d/2 < z \leqslant d. \end{cases} \qquad (75)$$

The solution for ϕ satisfies the second equation of (72). Therefore, using the approach detailed in Sec. VIII A, at leading order in $\mathrm{Er} \gg 1$, the thin-film Ericksen-Leslie equations (50)–(54) can now be written in terms of the unknown pressure $\tilde{p}$ as

$$u = \frac{1}{2\eta_L}\frac{\partial \tilde{p}}{\partial x}z(z-d),$$

$$v = \frac{1}{2\eta_L}\frac{\partial \tilde{p}}{\partial y}z(z-d),$$

$$w = \frac{d'}{d^3}(3d - 2z)z^2,$$

$$\frac{\partial^2 \tilde{p}}{\partial x^2} + \frac{\partial^2 \tilde{p}}{\partial y^2} = \frac{12\eta_L d'}{d^3},$$

$$\theta = \pm\theta_L, \quad \tan\phi = \frac{v}{u}, \qquad (76)$$

where $\eta_L = g(\theta_L) = g(-\theta_L)$ is the local effective viscosity of a flow-aligned nematic, which can be defined in terms of the Miesowicz viscosities as

$$\eta_L = \frac{\eta_1}{2}\left(1 - \frac{\gamma_1}{\gamma_2}\right) + \frac{\eta_2}{2}\left(1 + \frac{\gamma_1}{\gamma_2}\right) + \frac{\eta_{12}}{4}\left(1 - \frac{\gamma_1}{\gamma_2}\right)\left(1 + \frac{\gamma_1}{\gamma_2}\right). \qquad (77)$$

Therefore, we find that, at leading order in $\mathrm{Er} \gg 1$, the flow of a flow-aligning nematic is identical to the flow of an isotropic fluid with effective viscosity η_L, with the behavior of the director determined by the behavior of the flow; that is, the director lies in the plane that contains the flow direction and the direction of maximum shear stress, and aligns at the Leslie angle from the flow direction.

TABLE III. A summary of the thin-film Ericksen-Leslie equations (50)–(54) in the limit of large Ericksen number in terms of the unknown pressure $\tilde{p}$. Expressions for the tilt director angle θ, twist director angle ϕ, the equation governing the pressure $\tilde{p}$, and the velocities u, v, and w are stated.

	Large Ericksen number Er ≫ 1	
	Flow-aligning nematic (Sec. IX A)	Non-flow-aligning nematic (Sec. IX B)
θ	$\pm\theta_L$	0
ϕ	$\tan^{-1}\left(\dfrac{v}{u}\right)$	$\tan^{-1}\left(-\dfrac{u}{v}\right)$
$\tilde{p}$	$\dfrac{\partial^2 \tilde{p}}{\partial x^2} + \dfrac{\partial^2 \tilde{p}}{\partial y^2} = \dfrac{12\eta_L d'}{d^3}$	$\dfrac{\partial^2 \tilde{p}}{\partial x^2} + \dfrac{\partial^2 \tilde{p}}{\partial y^2} = \dfrac{12 d'}{d^3}$
u	$\dfrac{1}{2\eta_L}\dfrac{\partial \tilde{p}}{\partial x}(z-d)z$	$\dfrac{1}{2}\dfrac{\partial \tilde{p}}{\partial x}(z-d)z$
v	$\dfrac{1}{2\eta_L}\dfrac{\partial \tilde{p}}{\partial y}(z-d)z$	$\dfrac{1}{2}\dfrac{\partial \tilde{p}}{\partial y}(z-d)z$
w	$\dfrac{d'}{d^3}(3d - 2z)z^2$	

B. Non-flow-aligning nematics

For a non-flow-aligning nematic, the two solutions to (73) are

$$\tan\phi = -\frac{u}{v} \quad \text{with} \quad \theta = 0 \quad \text{or} \quad \theta = \frac{\pi}{2}. \qquad (78)$$

Of these two possibilities, the stable solution is $\theta = 0$ with $\tan\phi = -u/v$, known as the log-rolling solution [16], which has been studied in detail theoretically by Alonso et al. [66] and experimentally by Romo-Uribe and Windle [67]. Therefore, at leading order in $\mathrm{Er} \gg 1$, the thin-film Ericksen-Leslie equations (50)–(54) can be written in terms of the unknown pressure $\tilde{p}$ as

$$u = \frac{1}{2}\frac{\partial \tilde{p}}{\partial x}z(z-d),$$

$$v = \frac{1}{2}\frac{\partial \tilde{p}}{\partial y}z(z-d),$$

$$w = \frac{d'}{d^3}(3d - 2z)z^2,$$

$$\frac{\partial^2 \tilde{p}}{\partial x^2} + \frac{\partial^2 \tilde{p}}{\partial y^2} = \frac{12d'}{d^3},$$

$$\theta = 0, \quad \tan\phi = -\frac{u}{v}, \qquad (79)$$

and we find that, at leading order in $\mathrm{Er} \gg 1$, the flow of a non-flow-aligning nematic is identical to the flow of an isotropic fluid with unit effective viscosity, which corresponds to a dimensional viscosity η_3, with the behavior of the director determined by the behavior of the flow; that is, it aligns perpendicular to both the flow direction and the direction of maximum shear stress.

Table III summarizes the scenarios we have considered in the limit of large Ericksen number ($\mathrm{Er} \gg 1$).
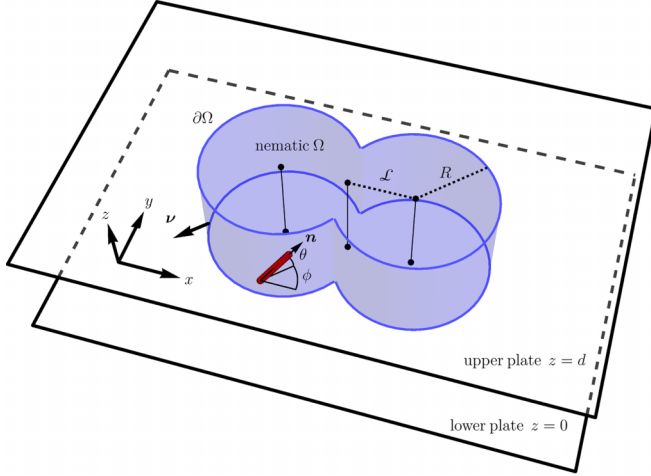
FIG. 2. A Hele-Shaw cell showing a perspective view of a region of nematic Ω with free surface $\partial\Omega$ with outward unit normal $\boldsymbol{\nu}$ defined by two overlapping cylindrical droplets (in light blue) bounded between solid parallel plates at $z = 0$ and $z = d$. The Cartesian coordinates x, y, and z, the tilt director angle θ, the twist director angle ϕ, the equal cylindrical radii R, the fixed half separation of the cylindrical droplets $\mathcal{L}$, the fixed axes of the cylindrical droplets $(-\mathcal{L}, 0, z)$ and $(\mathcal{L}, 0, z)$, and the fixed axis on which the center of mass lies $(0, 0, z)$ are also shown.

X. APPLICATION TO THE ONE-DROP-FILLING METHOD

As an example of the insight that can be gained by using the present theoretical approach, we calculate the flow that occurs during the squeezing of two coalescing nematic regions sandwiched between two parallel plates, as depicted in Fig. 2. This situation is a simple model for the squeezing stage of the ODF method, as discussed in Sec. I, in which regions of nematic are forcibly coalesced as an upper plate, located at $d(t)$, is moved towards a fixed lower plate, located at $z = 0$, In the present situation we assume that the decreasing gap between the plates is given, in dimensional form, by

$$d = d_0 - s_\mathrm{p} t \quad \text{for} \quad 0 \leqslant t \leqslant t_\mathrm{f}, \qquad (80)$$

where d_0 is the initial thickness of the cell, s_p is the speed at which the upper plate moves toward the lower plate, and $t_\mathrm{f} = (d_0 - d_\mathrm{f})/s_\mathrm{p}$ is the time at which the required final thickness of the cell d_f is achieved.

In the model presented in this section, we neglect any transient initial inertial effects at the start of the squeezing process and consider the two limiting cases of small and large Ericksen numbers. We also assume that the quasistatic evolution of the free surface $\partial\Omega = \partial\Omega(t)$ is prescribed using the solution of a conservation-of-volume model of two overlapping cylindrical nematic droplets $\Omega = \Omega(t)$. The model therefore neglects any effects that surface tension, elasticity, anchoring, and contact line dynamics might have on the evolution of the free surface. Specifically, we assume that the nematic region is the union of two cylindrical regions of nematic, having equal radii $R = R(t)$ and fixed axes $(-\mathcal{L}, 0, z)$ and $(\mathcal{L}, 0, z)$, with a combined constant volume V, and outward unit normal $\boldsymbol{\nu} = \boldsymbol{\nu}(x, y, t)$, as shown in Fig. 2. The center of mass of the nematic region lies on the fixed axis $(0, 0, z)$, and there are cusps in the

free surface formed where the overlapping cylinders meet at $(0, -c, z)$ and $(0, c, z)$, where $c = \sqrt{R(t)^2 - \mathcal{L}^2}$. The volume of the nematic region is then given by

$$\frac{V}{d} = \left[\pi - \cos^{-1}\left(\frac{\mathcal{L}}{R}\right)\right] R^2 + \mathcal{L}\sqrt{R(t)^2 - \mathcal{L}^2}, \qquad (81)$$

and, due to the conservation of volume, the evolution of the radius R, which determines the shape of the free surface $\partial\Omega$ is given implicitly by (81) [48]. The boundary condition for u and v on $\partial\Omega$ is then given by the kinematic condition

$$\boldsymbol{u} \cdot \boldsymbol{v} = R' \quad \text{on} \quad \partial\Omega, \qquad (82)$$

where $R' = \mathrm{d}R/\mathrm{d}t$ is the speed at which the free surface expands, which may be obtained via implicit differentiation of (81) with respect to t.

Free surfaces formed between a nematic and air (or vacuum) have been found to exhibit a variety of types of anchoring [51]. However, since homeotropic anchoring is the most commonly reported anchoring at free surfaces [51,53], and because this type of anchoring at a free surface is exhibited by a key component of modern nematic mixtures used in the ODF method, namely $4'$-pentyl-4-biphenylcarbonitrile (5CB) [65], we take the anchoring condition on $\partial\Omega$ to be homeotropic infinite anchoring, such that

$$\boldsymbol{v} \cdot \boldsymbol{n} = 1 \quad \text{on} \quad \partial\Omega. \qquad (83)$$

The anchoring conditions on the plates are assumed to be planar degenerate infinite anchoring (as discussed in Sec. VIII B 2). Note that, in the limit of large Ericksen number, which we will discuss shortly, the behavior of the director field is determined by the behavior of the flow in the bulk of the nematic region, and the anchoring conditions on the free surface and plates are not required.

An alternative approach to specifying the boundary conditions at the free surface $\partial\Omega$ could be to consider the balances of stress and torque as well as the kinematic condition on $\partial\Omega$. For example, considering the balance of normal stress on an isotropic free surface leads to the well-known isotropic Young-Laplace equation, which allows the effect of surface tension to influence the shape of the free surface [68,69]. The boundary conditions on a nematic free surface can be considerably more complex than in the isotropic case and involve the combined effects of surface tension, elasticity, anchoring, and contact line dynamics [58,70]. However, Cousins *et al.* [47] previously used the relatively simple model described above to make qualitative comparisons between theoretical predictions for the speed at which the free surface expands and experimental photographs of ODF mura, demonstrating that the timescale of coalescence due to surface tension effects is much longer than the timescale of the ODF squeezing process. This previous work did not calculate the flow or director field within the nematic region but, as we shall see shortly, this simple model of the free surface also leads to solutions for the director field that compare well to experimental results.

Before considering the limits of small and large Ericksen numbers, we introduce the appropriate nondimensionalization for the flow of nematic during the squeezing stage of the ODF method. In particular, we take the characteristic length scale in the z direction to be the initial separation of the plates

TABLE IV. Typical parameter values for the ODF method, specifically the initial thickness of the cell, d_0, the volume of the region consisting of two overlapping cylindrical nematic regions, V, the speed at which the upper plate moves downward towards the lower plate, s_p, the initial radius of each droplet, R_0, and the final thickness of the cell, d_f [47,48].

		Parameter		
d_0	V	s_p	R_0	d_f
Typical value 74.0 μm	4.5 μl	1.0 mm s^{-1}	4.4 mm	5.0 μm

$D = d_0$, the characteristic length scale in the xy plane to be half the separation of the droplets, which is also the initial radius of the cylindrical regions, $L = \mathcal{L} = R_0 = \sqrt{V/(\pi d_0)}$, and the characteristic velocity scale to be the velocity scale for a flow driven by squeezing a circular cylindrical volume V of nematic between parallel plates $U = S\sqrt{V/(4\pi D^3)}$, where the characteristic plate speed S is given by (80) as $S = s_p$. The aspect ratio δ, the Ericksen number Er, and the reduced Reynolds δRe can then be written in terms of d_0, s_p, V and the nematic material parameters, namely

$$\delta = \sqrt{\frac{\pi d_0^3}{V}}, \quad \mathrm{Er} = \frac{\mu s_p}{K}\sqrt{\frac{V}{4\pi d_0}}, \quad \text{and} \quad \delta\mathrm{Re} = \frac{\rho s_p d_0}{2\mu}. \tag{84}$$

Using the typical parameter values for the ODF method listed in Table IV and the parameters values of the nematic 5CB, namely $\mu = \eta_3 = 0.0326$ Pa s^{-1} and $K = 6.1$ pN [71], with (84) yields $\delta = 0.017$, Er $= 2.2 \times 10^3$, and δRe $= 0.017$. These values are consistent with those for the ODF method listed in Table I, as well as with the assumptions $\delta \ll 1$, δRe $\ll 1$ and Er $\gg 1$, and therefore the limit of large Ericksen number is likely to be the most appropriate. However, for completeness and to compare the two different limiting behaviors, we will also consider the behavior in the limit of small Ericksen number.

In order to allow comparison between our theoretical predictions and experimental results, we calculate an approximation to the (relative) optical transmission, denoted $T = T(x, y)$, through the droplets between crossed polarizers aligned with the x axis and the y axis, which is measured relative to the transmission of light when the component of the director $\boldsymbol{n}$ in the xy plane is aligned with one of the polarizers [72]. Since the director is either independent of z in the small Ericksen number limit (see Table II) or piecewise constant in the z direction in the high Ericksen number limit (see Table III), a simple approximation of the transmission is possible, and the relative optical transmission is given by $T = \sin^2 2\phi$ [72]. With this measure of transmission, 100% optical transmission occurs when the twist angle ϕ is $\pi/4$ or $3\pi/4$, i.e., when the component of $\boldsymbol{n}$ in the xy plane is $\pi/4$ from both polarizers, and 0% optical transmission occurs when the twist angle is 0 or $\pi/2$, i.e., when the component of $\boldsymbol{n}$ in the xy plane is aligned with one of the polarizers.

A. The limit of small Ericksen number

In the limit of small Ericksen number (Er $\ll 1$), and with planar degenerate anchoring on the plates, the appropriate equations are provided in the final column of Table II. We proceed by first solving Laplace's equation for the twist angle ϕ given by (71) subject to the anchoring condition (83), and then solving the equation for the pressure $\tilde{p}$ given by (71) subject to the kinematic condition (82). We note that (68) and (83) can be solved analytically using a conformal mapping from two intersecting circles to the half-plane; however, this approach leads to integrals that must be evaluated numerically, and so there is little advantage of pursuing this approach over a purely numerical approach. We therefore use COMSOL Multiphysics [73] to numerically solve (68) and (83) for the twist director angle ϕ, and subsequently numerically solve Eq. (71) for the pressure $\tilde{p}$. Once the solutions for ϕ and $\tilde{p}$ are determined, the expressions for u and v in (71) determine the velocity. From (71) we see that a nonuniform solution for the director field will lead to an anisotropic patterned viscosity via the effective viscosity functions β_1, β_2, and β_3, which themselves depend on the nondimensional viscosity η_1 (equal to the ratio of dimensional viscosities η_1/η_3). The flow is driven by the squeezing together of the plates but guided by the patterned viscosity. Note that, in the special case that the dimensional viscosities η_1 and η_3 are equal, the director does not affect the flow.

Figure 3 shows the numerically calculated solutions for pressure $\tilde{p}$ and the director field $\boldsymbol{n}$ [the top row, (a)–(c)], as well as the speed $|\boldsymbol{u}|$ and streamlines [the middle row, (d)–(f)], and the optical transmission [the bottom row, (g)–(i)] at leading order in the limit of small Ericksen number (Er $\ll 1$) for the parameters listed in Table IV at three different times: the first column, (a), (d), and (g), for $t = 0.02$ s when $d = 54$ μm and $R' = 0.05$ m s^{-1}; the second column, (b), (e), and (h), for $t = 0.04$ s when $d = 34$ μm and $R' = 0.12$ m s^{-1}; and the third column, (c), (f), and (i), for $t = 0.06$ s when $d = 14$ μm and $R' = 0.49$ m s^{-1}. Note that, since the director field is fixed by the infinite anchoring on the free surface, there is a discontinuity in the director field at the cusp located at $(0, -c)$. The symmetry of the system means that there is another solution with a defect at the cusp at $(0, c)$, which is a reflection of the solution in Fig. 3 in the line through the centers of the cylinders. There are also higher energy solutions that satisfy (68) and (83), including a solution with defects at both cusps, but these solutions are unlikely to occur in practice due to their higher energy. Asymmetry in the director field solution leads to asymmetry in the effective viscosity, and then to asymmetry in the pressure $\tilde{p}$ and the velocity, shown by the streamlines in Figs. 3(d)–3(f). Figures 3(g)–3(i) show the optical transmission T in the limit of small Er and provides a visualization of the director field that can be readily be compared to the optical transmission observed in experiments.

B. The limit of large Ericksen number

For the limit of large Ericksen number (Er $\gg 1$), which is probably more appropriate to the ODF method than the limit of small Ericksen number discussed in Sec. X A, we consider flow-aligning nematics [50], again the most relevant choice for the materials used in the ODF method. In this
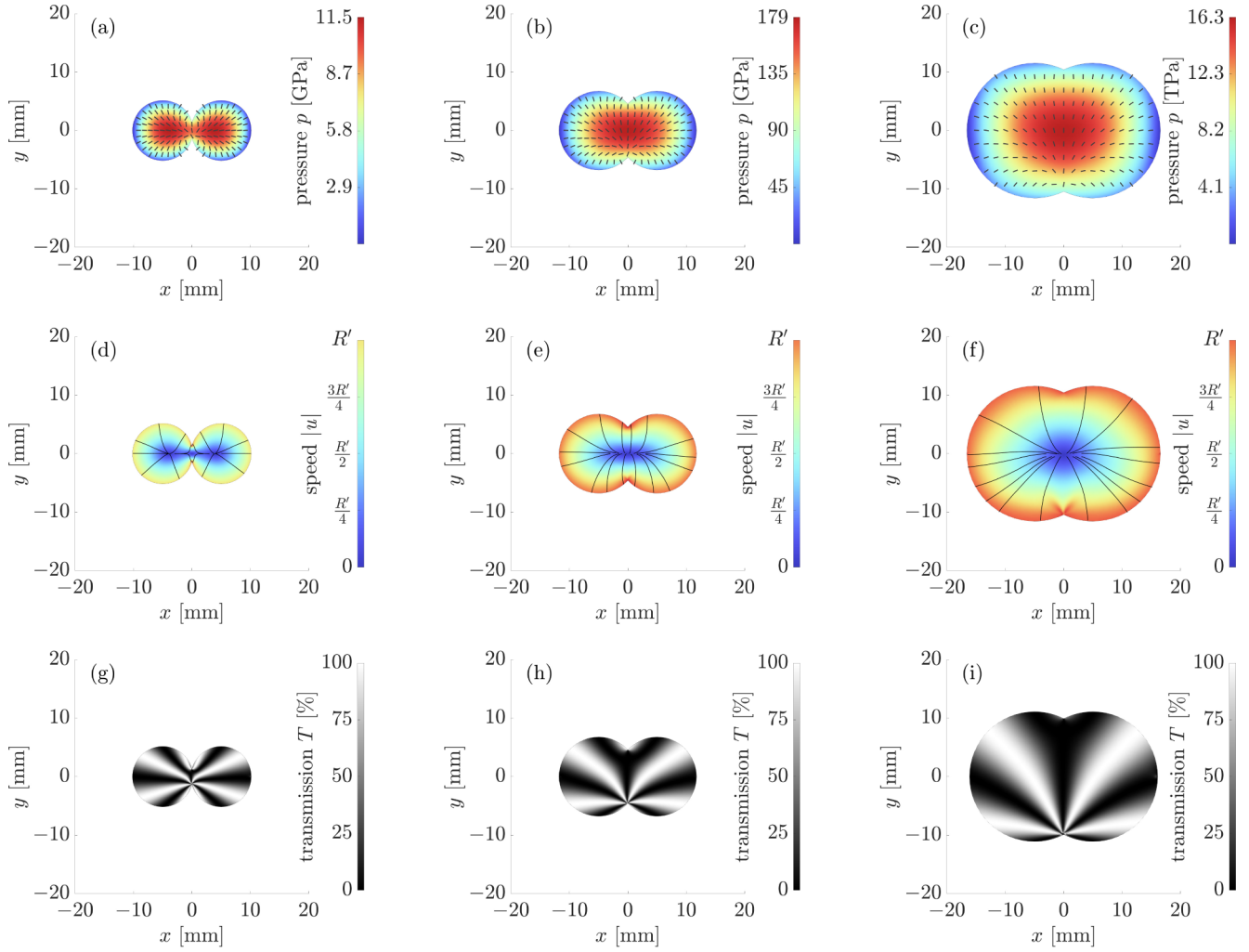
FIG. 3. Top row (a)–(c): the pressure $\tilde{p}$ (colored background) and the director field $\boldsymbol{n}$ (black rods); middle row (d)–(f): flow speed $|\boldsymbol{u}|$ (colored background) and streamlines (solid black lines); bottom row (g)–(i): the optical transmission T (greyscale), in the limit of small Ericksen number (Er $\ll 1$) for two coalescing droplets at $t = 0.02$ s when $d = 54$ μm and $R' = 0.05$ m s^{-1} [first column, (a), (d), and (g)]; $t = 0.04$ s when $d = 34$ μm and $R' = 0.12$ m s^{-1} [second column, (b), (e), and (h)]; and $t = 0.06$ s when $d = 14$ μm and $R' = 0.49$ m s^{-1} [third column, (c), (f), and (i)].

case, at leading order the director is determined by the flow, and hence the anchoring conditions on both the free surface and the plates are not satisfied, the anchoring being broken by the flow effects. Specifically, the torque on the director at the free surface and the plates due to anchoring forces is overcome by the torque due to flow effects, and the resulting director orientation is determined entirely by the flow. This phenomenon is a flow-induced type of anchoring breaking that has been discussed in the context of channel flow by Cousins *et al.* [50].

The solution in the limit of large Ericksen number for a flow-aligning nematic can be obtained from the equations given in the first column of Table III, with the solution to Poisson's equation for the pressure, which is given in (76), subject to the kinematic condition (82) also providing the solutions for the velocities and twist director angle. Similarly to Sec. X A, we note that (76) and (82) can be solved analytically using a conformal mapping (see [68,69] for more details); however, this approach again leads to integrals that must be

evaluated numerically, and so again there is little advantage of pursuing this approach over a purely numerical approach. We therefore again use COMSOL Multiphysics [73] to numerically solve the Poisson equation for the pressure in (76).

Figure 4 shows the numerically calculated solutions for pressure $\tilde{p}$ and the director field $\boldsymbol{n}$ [the top row, (a)–(c)], as well as the speed $|\boldsymbol{u}|$ and streamlines [the middle row, (d)–(f)], and the optical transmission T [the bottom row, (g)–(i)] at leading order in the limit of large Ericksen number (Er $\gg 1$) for the parameters listed in Table IV at three different times: the first column, (a), (d), and (g), for $t = 0.02$ s when $d = 54$ μm and $R' = 0.05$ m s^{-1}; the second column, (b), (e), and (h), for $t = 0.04$ s when $d = 34$ μm and $R' = 0.12$ m s^{-1}; and the third column, (c), (f), and (i), for $t = 0.06$ s when $d = 14$ μm and $R' = 0.49$ m s^{-1}. The pressure $\tilde{p}$ shown in Figs. 4(a)–4(c) initially attains a local maximum at the center of each droplet, and as t increases, and hence as d decreases, the maximum in the pressure moves towards the center of the two coalescing droplets. Figures 4(d)–4(f) show that at $t =$
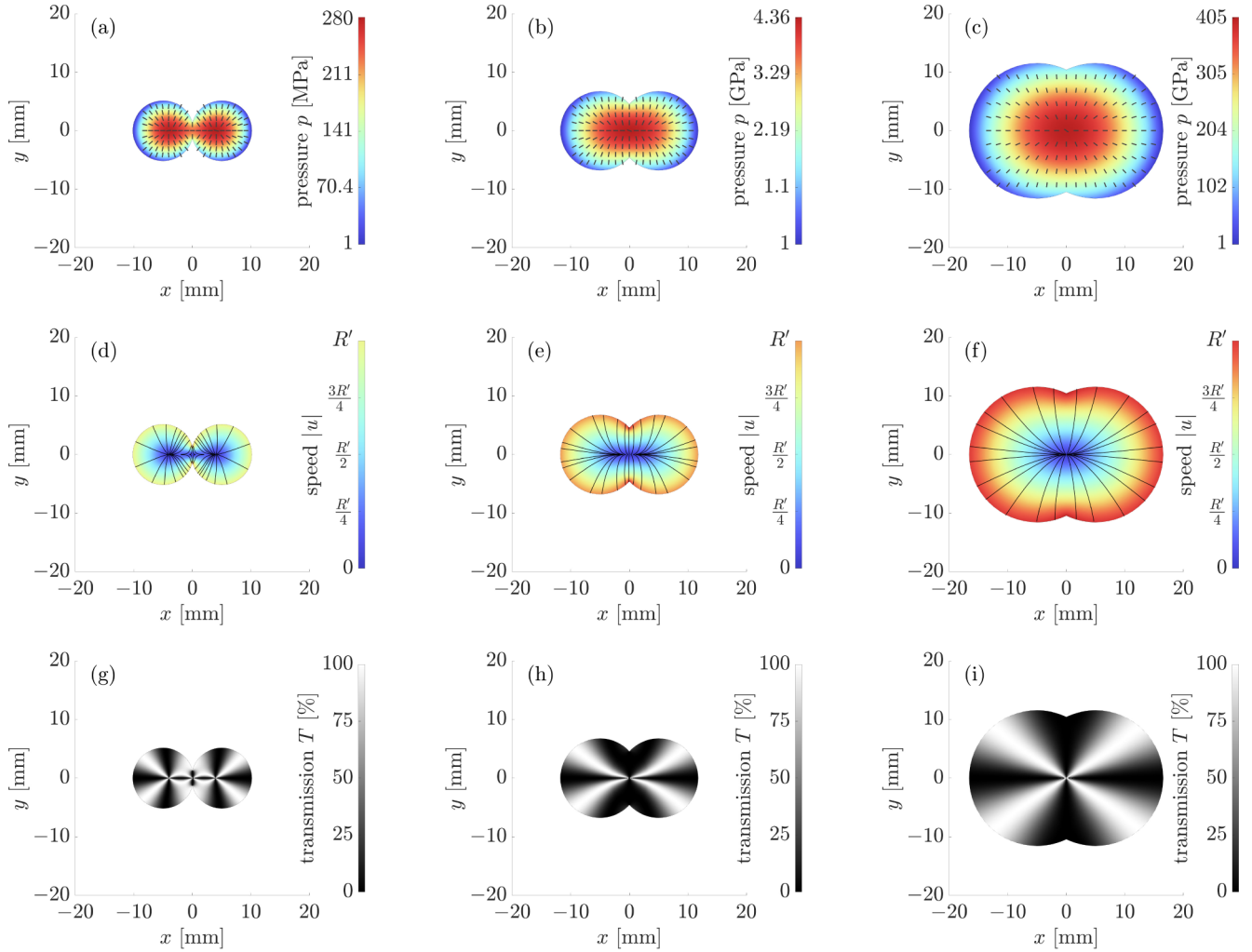
FIG. 4. Top row (a)–(c): the pressure $\tilde{p}$ (coloured background) and the director field $\boldsymbol{n}$ (black rods); middle row (d)–(f): flow speed $|\boldsymbol{u}|$ (coloured background) and streamlines (solid black lines); bottom row (g)–(i): the optical transmission T (greyscale), in the limit of large Ericksen number (Er $\gg 1$) for two coalescing droplets at $t = 0.02$ s when $d = 54$ μm and $R' = 0.05$ m s^{-1} [first column, (a), (d), and (g)]; $t = 0.04$ s when $d = 34$ μm and $R' = 0.12$ m s^{-1} [second column, (b), (e), and (h)]; and $t = 0.06$ s when $d = 14$ μm and $R' = 0.49$ m s^{-1} [third column, (c), (f), and (i)].

0.02 s the streamlines form two radial distributions with the streamline origins located at the maxima in the pressure, and as t increases and the two maxima in the pressure approach the center of the coalescing droplets, the streamlines approach a single radial distribution with the streamline origins located at the center of the coalescing droplets. As expected, the director field $\boldsymbol{n}$ shown in Figs. 4(a)–4(c) is determined by the flow and hence aligns with the streamlines shown in Figs. 4(d)–4(f). Finally, Figs. 4(g)–4(i) show the optical transmission T in which a $+1$ defect is positioned at the center of each of the two coalescing droplets and a -1 defect is positioned at the center of the two coalescing droplets [19]. As t increases, and hence as d decreases, the defects move towards the center of the two coalescing droplets and merge. Again, the optical transmission shown in Figs. 4(g)–4(i) provides a visualization of the director field that can be readily compared to the optical transmission observed in experiments.

XI. CONCLUSIONS

In the present work, we considered the flow of a nematic in a standard Hele-Shaw cell that consists of two parallel plates, one of which may move in the direction perpendicular to the plates, separated by a narrow gap which is partially or wholly filled with the nematic.

In Secs. II to VII, we derived the thin-film Ericksen-Leslie equations that govern the flow and director within a nematic Hele-Shaw cell. The thin-film Ericksen Leslie equations are given by the conservation of mass equation (49), the conservation of linear momentum equations (50) and (51), and the conservation of angular momentum equations (53) and (54) subject to the no-slip and no-penetration conditions on the plates (41) and (42) and we chose two general anchoring conditions described in Sec. IV that are relevant to a variety of situations. These governing equations may, in principle, be generalized to include conservative body forces and other
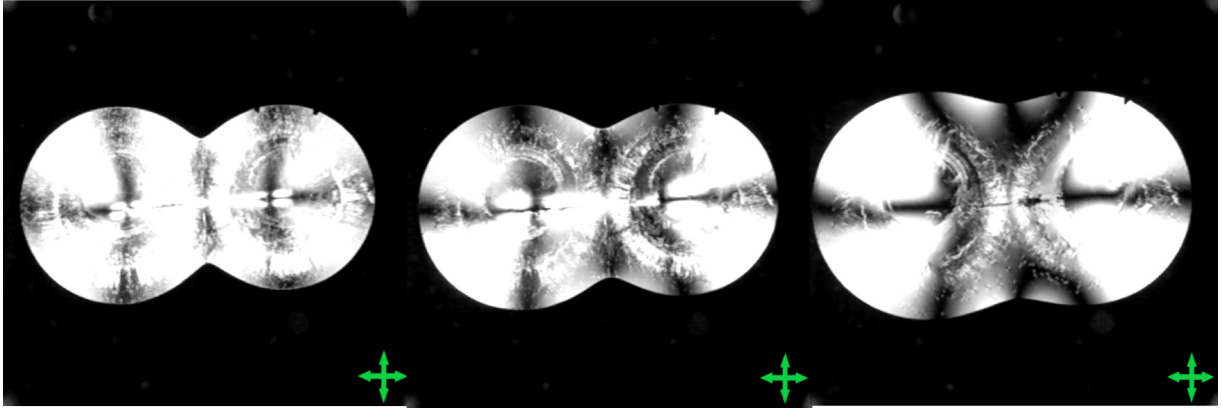
FIG. 5. Experimental photographs of the optical transmission of light through a two-droplet ODF test setup between crossed polarizers by Merck KGaA using an unknown nematic material or nematic mixture (with polarizer direction indicated by the green arrows). Left to right shows the increase of time. Regions of white show complete optical transmission through the droplets and regions of black show no optical transmission. (Photographs provided by Merck KGaA.)

choices of boundary conditions on the plates and/or the free surface $\partial\Omega$.

In Secs. VIII and IX, we solved the thin-film Ericksen-Leslie equations in the limits of small and large Ericksen numbers. In the limit of small Ericksen number, the anchoring pattern on the plates determines the director field throughout the cell, and therefore the director field is fixed. The fixed director field produces an anisotropic patterned viscosity. In particular, in the cases of unidirectional rubbed infinite anchoring with a constant pretilt and axisymmetric infinite anchoring with a constant pretilt, the flow is guided along the rubbing direction and guided by the axisymmetric anchoring pattern leading to a spiral flow, respectively. Mi and Yang [15] and Sengupta [36] experimentally observed a reduction in the velocity of a nematic capillary flow when the flow was perpendicular to the rubbing direction compared to when the flow was parallel to the rubbing direction. Analogous behavior has also been observed in spreading nematic droplets on rubbed surfaces, both experimentally by Tortora and Lavrentovich [74] and in molecular dynamics simulations by Vanzo *et al.* [75], where elongation of the droplet free surface is guided by the rubbing direction, which leads to ellipsoidal nematic droplets known as tactoids. In the limit of large Ericksen number, there are two cases, either the nematic is a flow-aligning nematic or the nematic is a non-flow-aligning nematic. In both of these cases, the flow is identical to the flow of an isotropic fluid, and the behavior of the director is determined by the flow. Summaries of the thin-film Ericksen-Leslie equations in the limits of small and large Ericksen numbers are given in Tables II and III, respectively.

Finally, in Sec. X, we applied the results of the limits of small and large Ericksen numbers to a simple model for the squeezing stage of the ODF method. The optical transmission calculated in these limits, shown in Figs. 3(g)–3(i) and 4(g)–4(i), respectively, provides a clear visualization of the director field which can be compared to the optical transmission observed in experiments. The optical transmission of light measured through a two-droplet ODF test setup by Merck KGaA using an unknown nematic material or nematic mixture is shown in Fig. 5. Visual comparison of the experimental photographs and the results of the present theoretical model in the limit of large Ericksen number shown in Figs. 4(g)–4(i) show a striking resemblance, suggesting that the present theoretical model may provide a useful description of the ODF method. We also note that it is clear from the experimental photographs shown in Fig. 5 that the droplets remain approximately cylindrical, justifying our modeling assumption that surface tension effects can be neglected.

We anticipate that many other nematic systems, including experiments on nematic viscous fingering and nematic microfluidics, can also be analyzed using the thin-film Ericksen-Leslie equations derived in the present work, thus providing computationally cheaper models (which in some special cases allow for analytical solutions) than fully numerical alternatives, for studying flow in nematic Hele-Shaw cells.

APPENDIX A: NEMATIC VISCOUS DISSIPATION

The standard nematic viscous dissipation $\mathcal{D}$ [16], given by (11), is obtained using the velocity and director in the form of (1) and (3), respectively, with the definitions of the corotational time flux of the director N and the rate of strain tensor A mentioned in the text. The components are summarized here:

$$
(\boldsymbol{n} \cdot \boldsymbol{A}\,\boldsymbol{n})^2 = [\cos^2\phi\cos^2\theta\,u_x + \cos^2\theta\cos\phi\sin\phi(u_y + v_x) + \cos^2\theta\sin^2\phi\,v_y + \cos\phi\cos\theta\sin\theta(u_z + w_x)
$$
$$
+ \cos\theta\sin\phi\sin\theta(v_z + w_y) + \sin^2\theta\,w_z]^2, \tag{A1}
$$

$$
\boldsymbol{N} \cdot \boldsymbol{A}\,\boldsymbol{n} = \tfrac{1}{4}[-2\cos\phi\cos\theta u_x(2\cos\theta\dot{\phi}\sin\phi + 2\cos\phi\dot{\theta}\sin\theta + \cos\theta\sin\phi u_y + \sin\theta u_z - \cos\theta\sin\phi v_x - \sin\theta w_x)
$$
$$
- \cos\theta\sin\phi(u_y + v_x)(2\cos\theta\dot{\phi}\sin\phi + 2\cos\phi\dot{\theta}\sin\theta + \cos\theta\sin\phi u_y + \sin\theta u_z - \cos\theta\sin\phi v_x - \sin\theta w_x)
$$
$$
- \sin\theta(u_z + w_x)(2\cos\theta\dot{\phi}\sin\phi + 2\cos\phi\dot{\theta}\sin\theta + \cos\theta\sin\phi u_y + \sin\theta u_z - \cos\theta\sin\phi v_x - \sin\theta w_x)
$$
$$
+ \cos^2\theta(\cos\phi(u_z + w_x) + \sin\phi(v_z + w_y))(2\dot{\theta} + \cos\phi u_z + \sin\phi v_z - \cos\phi w_x - \sin\phi w_y)
$$
$$
- \sin\theta(v_z + w_y)(-2\cos\phi\cos\theta\dot{\phi} + 2\dot{\theta}\sin\phi\sin\theta - \cos\phi\cos\theta u_y + \cos\phi\cos\theta v_x + \sin\theta v_z - \sin\theta w_y)
$$
$$
+ \cos\phi\cos\theta(u_y + v_x)(2\cos\phi\cos\theta\dot{\phi} - 2\dot{\theta}\sin\phi\sin\theta + \cos\phi\cos\theta u_y - \cos\phi\cos\theta v_x - \sin\theta v_z + \sin\theta w_y)
$$
$$
+ 2\cos\theta\sin\phi v_y(2\cos\phi\cos\theta\dot{\phi} - 2\dot{\theta}\sin\phi\sin\theta + \cos\phi\cos\theta u_y - \cos\phi\cos\theta v_x - \sin\theta v_z + \sin\theta w_y)
$$
$$
+ 2\cos\theta\sin\theta(2\dot{\theta} + \cos\phi u_z + \sin\phi v_z - \cos\phi w_x - \sin\phi w_y)w_z], \tag{A2}
$$

$$
\mathrm{tr}(\boldsymbol{A}^2) = \tfrac{1}{2}\big[2u_x^2 + (u_y + v_x)^2 + 2v_y^2 + (u_z + w_x)^2 + (v_z + w_y)^2 + 2w_z^2\big], \tag{A3}
$$

$$
(\boldsymbol{A}\,\boldsymbol{n})^2 = \tfrac{1}{4}\big[4\cos^2\phi\cos^2\theta\,u_x^2 + 4\cos^2\theta\cos\phi\sin\phi\,u_x(u_y + v_x) + \cos^2\phi\cos^2\theta(u_y + v_x)^2
$$
$$
+ \cos^2\theta\sin^2\phi(u_y + v_x)^2 + 4\cos^2\theta\cos\phi\sin\phi(u_y + v_x)v_y + 4\cos^2\theta\sin^2\phi\,v_y^2
$$
$$
+ 4\cos\phi\cos\theta\sin\theta\,u_x(u_z + w_x) + 2\cos\theta\sin\phi\sin\theta(u_y + v_x)(u_z + w_x)
$$
$$
+ \cos^2\phi\cos^2\theta(u_z + w_x)^2 + \sin^2\theta(u_z + w_x)^2 + 2\cos\phi\cos\theta\sin\theta(u_y + v_x)(v_z + w_y)
$$
$$
+ 4\cos\theta\sin\phi\sin\theta\,v_y(v_z + w_y) + 2\cos^2\theta\cos\phi\sin\phi(u_z + w_x)(v_z + w_y) + \cos^2\theta\sin^2\phi(v_z + w_y)^2
$$
$$
+ \sin^2\theta(v_z + w_y)^2 + 4\cos\phi\cos\theta\sin\theta(u_z + w_x)w_z
$$
$$
+ 4\cos\theta\sin\phi\sin\theta(v_z + w_y)w_z + 4\sin^2\theta w_z^2\big], \tag{A4}
$$

$$
\boldsymbol{N}^2 = \tfrac{1}{4}\big[(2\cos\theta\dot{\phi}\sin\phi + 2\cos\phi\dot{\theta}\sin\theta + \cos\theta\sin\phi\,u_y + \sin\theta\,u_z - \cos\theta\sin\phi\,v_x - \sin\theta\,w_x)^2
$$
$$
+ \cos^2\theta(2\dot{\theta} + \cos\phi\,u_z + \sin\phi\,v_z - \cos\phi\,w_x - \sin\phi\,w_y)^2
$$
$$
+ (2\cos\phi\cos\theta\dot{\phi} - 2\dot{\theta}\sin\phi\sin\theta + \cos\phi\cos\theta\,u_y - \cos\phi\cos\theta\,v_x - \sin\theta\,v_z + \sin\theta\,w_y)^2\big], \tag{A5}
$$

where partial derivatives are denoted with subscripts, so that, for example, $u_x = \partial u/\partial x$.

APPENDIX B: TYPICAL PARAMETER VALUES

The values of the timescales τ_1, τ_2, and τ_3 and nondimensional numbers δ, Re, and Er in Table I are calculated from (38), (39), (46), (25), (40), and (45), respectively, with the typical parameter values stated below.

Analysis of the ODF method was carried out by Cousins *et al.* [49] for a range of present and possible future length scales, depths and upper plate speeds given by $L = 50\ \mu\mathrm{m}$–5 mm, depths $D = 50\ \mu\mathrm{m}$–0.5 μm, and plate speeds 2 $\mu\mathrm{m\,s^{-1}}$–1 mm s^{-1} (which yields a velocity scale in the range $U = 0.0002$–0.1 m s^{-1}), respectively. Typical values for the nematic isotropic viscosity $\mu = 0.01$ Pa s, one-constant elastic constant $K = 10$ pN, and density $\rho = 1000$ kg m^{-3} are also used.

Capillary-filling experiments were carried out by Mi and Yang [15] for the nematic 5CB in rectangular channels of length $L = 0.1$ m, depth $D = 10\ \mu$m, with front propagation speed of $U = 0.01$ cm s^{-1} for the nematic 5CB [15].

Air-nematic viscous fingering experiments were carried out by Sonin and Bartolino [21] for the nematic 5CB by lifting the upper plate of a Hele-Shaw cell of length $L = 0.1$ mm, depth $D = 3.5\ \mu$m, upward plate speed 280 μm s^{-1} (which yields a velocity scale of $U = 8$ mm s^{-1}).

Microfluidic experiments in channels containing a micropillar were carried out by Sengupta *et al.* [34] for the nematic 5CB in channels of length $L = 20$ mm, with a range of depths $D = 8$–50 μm and flow velocities $U = 200$–670 μm s^{-1}.

[1] H. S. Hele-Shaw, The flow of water, Nature (London) **58**, 34 (1898).

[2] G. G. Stokes, Mathematical proof of the identity of the stream lines obtained by means of a viscous film with those of a perfect fluid moving in two dimensions, in *Report of the Sixty-Eighth Meeting of the British Association for the Advancement of Science* (Cambridge University Press, Cambridge, 1898), pp. 143–144.

[3] D. J. Acheson, *Elementary Fluid Dynamics* (Oxford University Press, Oxford, 1990).

[4] P. G. Saffman and G. I. Taylor, The penetration of a fluid into a porous medium or Hele-Shaw cell containing a more viscous liquid, Proc. R. Soc. London A **245**, 312 (1958).

[5] P. G. Saffman, Viscous fingering in Hele-Shaw cells, J. Fluid Mech. **173**, 73 (1986).

[6] S. D. Howison, Bubble growth in porous media and Hele-Shaw cells, Proc. R. Soc. Edinburgh: Sect. A Math. **102**, 141 (1986).

[7] H. E. Huppert and A. W. Woods, Gravity-driven flows in porous layers, J. Fluid Mech. **292**, 55 (1995).

[8] G. M. Homsy, Viscous fingering in porous media, Annu. Rev. Fluid Mech. **19**, 271 (1987).

[9] A. R. Kopf-Sill and G. M. Homsy, Bubble motion in a Hele-Shaw cell, Phys. Fluids **31**, 18 (1988).

[10] S. Tanveer and P. G. Saffman, Stability of bubbles in a Hele-Shaw cell, Phys. Fluids **30**, 2624 (1987).

[11] S. D. Howison, Bibliography of free and moving boundary problems in Hele-Shaw and Stokes flow, https://people.maths.ox.ac.uk/howison/Hele-Shaw/, last updated 18 August 1998.

[12] L. C. Morrow, T. J. Moroney, M. C. Dallaston, and S. W. McCue, A review of one-phase Hele-Shaw flows and a level-set method for nonstandard configurations, ANZIAM J. **63**, 269 (2021).

[13] O. Hassager and T. L. Lauridsen, Singular behavior of power-law fluids in Hele Shaw flow, J. Non-Newtonian Fluid Mech. **29**, 337 (1988).

[14] J. S. Ro and G. M. Homsy, Viscoelastic free surface flows: thin film hydrodynamics of Hele-Shaw and dip coating flows, J. Non-Newtonian Fluid Mech. **57**, 203 (1995).

[15] X.-D. Mi and D.-K. Yang, Capillary filling of nematic liquid crystals, Phys. Rev. E **58**, 1992 (1998).

[16] I. W. Stewart, *The Static and Dynamic Continuum Theory of Liquid Crystals* (Taylor & Francis, Oxford, 2004).

[17] J. L. Ericksen, Anisotropic fluids, Arch. Ration. Mech. Anal. **4**, 231 (1959).

[18] F. M. Leslie, Some constitutive equations for anisotropic fluids, Q. J. Mech. Appl. Math. **19**, 357 (1966).

[19] P. G. de Gennes and J. Prost, *The Physics of Liquid Crystals* (Oxford University Press, Oxford, 1993).

[20] A. Buka, J. Kertész, and T. Vicsek, Transitions of viscous fingering patterns in nematic liquid crystals, Nature (London) **323**, 424 (1986).

[21] A. A. Sonin and R. Bartolino, Air viscous fingers in isotropic fluid and liquid crystals obtained in lifting Hele-Shaw cell geometry, Nuovo Cimento D **15**, 1 (1993).

[22] L. Lam, H. C. Morris, R. F. Shao, S. L. Yang, Z. C. Liang, S. Zheng, and H. Liu, Dynamics of viscous fingers in Hele-Shaw cells of liquid crystals: Theory and experiment, Liq. Cryst. **5**, 1813 (1989).

[23] L. Lam, R. D. Freimuth, and H. S. Lakkaraju, Fractal patterns in burned Hele-Shaw cells of liquid crystals and oils, Mol. Cryst. Liq. Cryst. **199**, 249 (1991).

[24] R. Folch, J. Casademunt, and A. Hernández-Machado, Viscous fingering in liquid crystals: Anisotropy and morphological transitions, Phys. Rev. E **61**, 6632 (2000).

[25] R. Folch, T. Tóth-Katona, Á. Buka, J. Casademunt, and A. Hernández-Machado, Periodic forcing in viscous fingering of a nematic liquid crystal, Phys. Rev. E **64**, 056225 (2001).

[26] T. Tóth-Katona and Á. Buka, Nematic-liquid-crystal–air interface in a radial Hele-Shaw cell: Electric field effects, Phys. Rev. E **67**, 041717 (2003).

[27] A. Sengupta, S. Herminghaus, and C. Bahr, Liquid crystal microfluidics: surface, elastic and viscous interactions at microscales, Liq. Cryst. Rev. **2**, 73 (2014).

[28] A. Sengupta, U. Tkalec, and C. Bahr, Nematic textures in microfluidic environment, Soft Matter **7**, 6542 (2011).

[29] A. Sengupta, S. Herminghaus, and C. Bahr, Opto-fluidic velocimetry using liquid crystal microfluidics, Appl. Phys. Lett. **101**, 164101 (2012).

[30] A. Sengupta, U. Tkalec, M. Ravnik, J. M. Yeomans, C. Bahr, and S. Herminghaus, Liquid crystal microfluidics for tunable flow shaping, Phys. Rev. Lett. **110**, 048303 (2013).

[31] L. Giomi, Ž. Kos, M. Ravnik, and A. Sengupta, Cross-talk between topological defects in different fields revealed by nematic microfluidics, Proc. Natl. Acad. Sci. USA **114**, E5771 (2017).

[32] A. Sengupta, C. Bahr, and S. Herminghaus, Topological microfluidics for flexible micro-cargo concepts, Soft Matter **9**, 7251 (2013).

[33] A. S. Bhadwal, N. J. Mottram, A. Saxena, I. C. Sage, and C. V. Brown, Electrically controlled topological micro cargo transportation, Soft Matter **16**, 2961 (2020).

[34] A. Sengupta, C. Pieper, J. Enderlein, C. Bahr, and S. Herminghaus, Flow of a nematogen past a cylindrical micropillar, Soft Matter **9**, 1937 (2013).

[35] T. Stieger, H. Agha, M. Schoen, M. G. Mazza, and A. Sengupta, Hydrodynamic cavitation in Stokes flow of anisotropic fluids, Nat. Commun. **8**, 15550 (2017).

[36] A. Sengupta, Tuning fluidic resistance via liquid crystal microfluidics, Int. J. Mol. Sci. **14**, 22826 (2013).

[37] Y.-J. Na, T.-Y. Yoon, S. Park, B. Lee, and S.-D. Lee, Electrically programmable nematofluidics with a high level of selectivity in a hierarchically branched architecture, ChemPhysChem **11**, 101 (2010).

[38] T. G. Anderson, E. Mema, L. Kondic, and L. J. Cummings, Transitions in Poiseuille flow of nematic liquid crystal, Int. J. Non Linear Mech. **75**, 15 (2015).

[39] M. Crespo, A. Majumdar, A. M. Ramos, and I. M. Griffiths, Solution landscapes in nematic microfluidics, Physica D **351–352**, 1 (2017).

[40] V. M. O. Batista, M. L. Blow, and M. M. Telo da Gama, The effect of anchoring on the nematic flow in channels, Soft Matter **11**, 4674 (2015).

[41] A. Sharma, I. L. H. Ong, and A. Sengupta, Time dependent lyotropic chromonic textures in microfluidic confinements, Crystals **11**, 35 (2021).

[42] V. Ulaganathan and A. Sengupta, Spatio-temporal programming of lyotropic phase transition in nanoporous microfluidic confinements, J. Colloid Interface Sci. **649**, 302 (2023).

[43] H. Kamiya, K. Tajima, K. Toriumi, K. Terada, H. Inoue, T. Yokoue, N. Shimizu, T. Kobayashi, S. Odahara, G. Hougham, C. Cai, J. H. Glownia, R. J. von Gutfeld, R. John, and S.-C. A. Lien, 56.3: Development of one drop fill technology for AM-LCDs, Soc. Inf. Disp. Int. Symp. Dig. Tech. Pap. **32**, 1354 (2001).

[44] Y. Yamamoto, LCD processing and testing, in *Handbook of Visual Display Technology*, edited by J. Chen, W. Cranton, and M. Fihn (Springer, Berlin, 2012), Chap. 7.6.1, pp. 1649–1671.

[45] H. Lee, S. Song, J. Lee, A. Xiao, T. Min, and S. Su, 9.3: Analysis of liquid crystal drop mura in high resolution mobile thin film transistor liquid crystal displays, Soc. Inf. Disp. Int. Symp. Dig. Tech. Pap. **45**, 97 (2014).

[46] W. K. Pratt, S. S. Sawkar, and K. O'Reilly, Automatic blemish detection in liquid crystal flat panel displays, Proc. SPIE **3306**, 1 (1998).

[47] J. R. L. Cousins, S. K. Wilson, N. J. Mottram, D. Wilkes, L. Weegels, and K. Lin, LCT8-4: A model for the formation of mura during the one-drop-filling process, in *Proceedings of the 25th International Display Workshops (IDW 2018)* (Society for Information Display, Tokyo, 2018), Vol. 1, pp. 125–127.

[48] J. R. L. Cousins, Mathematical modelling and analysis of industrial manufacturing of liquid crystal displays, Ph.D. thesis, University of Strathclyde, 2021.

[49] J. R. L. Cousins, S. K. Wilson, N. J. Mottram, D. Wilkes, and L. Weegels, Squeezing a drop of nematic liquid crystal with strong elasticity effects, Phys. Fluids **31**, 083107 (2019).

[50] J. R. L. Cousins, S. K. Wilson, N. J. Mottram, D. Wilkes, and L. Weegels, Transient flow-driven distortion of a nematic liquid crystal in channel flow with dissipative weak planar anchoring, Phys. Rev. E **102**, 062703 (2020).

[51] A. A. Sonin, *The Surface Physics of Liquid Crystals* (Gordon & Breach, Oxford, 1995).

[52] V. Chigrinov, A. Kudreyko, and Q. Guo, Patterned photoalignment in thin films: Physics and applications, Crystals **11**, 84 (2021).

[53] J. R. L. Cousins, A. S. Bhadwal, L. T. Corson, B. R. Duffy, I. C. Sage, C. V. Brown, N. J. Mottram, and S. K. Wilson, Weak-anchoring effects in a thin pinned ridge of nematic liquid crystal, Phys. Rev. E **107**, 034702 (2023).

[54] W. M. Gibbons, P. J. Shannon, S.-T. Sun, and B. J. Swetlin, Surface-mediated alignment of nematic liquid crystals with polarized laser light, Nature (London) **351**, 49 (1991).

[55] L. P. Jones, Alignment properties of liquid crystals, in *Handbook of Visual Display Technology*, edited by J. Chen, W. Cranton, and M. Fihn (Springer, Berlin, 2012), Chap. 7.2.2, pp. 1387–1402.

[56] K. Hanaoka, Y. Nakanishi, Y. Inoue, S. Tanuma, Y. Koike, and K. Okamoto, 40.1: A new MVA-LCD by polymer sustained alignment technology, Soc. Inf. Disp. Int. Symp. Dig. Tech. Pap. **35**, 1200 (2004).

[57] H.-Y. Wu and R.-P. Pan, Liquid crystal surface alignments by using ion beam sputtered magnetic thin films, Appl. Phys. Lett. **91**, 074102 (2007).

[58] J. R. L. Cousins, B. R. Duffy, S. K. Wilson, and N. J. Mottram, Young and Young–Laplace equations for a static ridge of nematic liquid crystal, and transitions between equilibrium states, Proc. R. Soc. A **478**, 20210849 (2022).

[59] M. A. Lam, L. J. Cummings, T.-S. Lin, and L. Kondic, Three-dimensional coating flow of nematic liquid crystal on an inclined substrate, Eur. J. Appl. Math. **26**, 647 (2015).

[60] S.-C. Zhao, C.-L. Yuan, Y.-F. Wang, P.-Z. Sun, B.-H. Liu, H.-L. Hu, D. Shen, and Z.-G. Zheng, Anisotropic microfluidics and flow monitoring with a microchannel towards soft-matter sensing, J. Mater. Chem. C **10**, 11767 (2022).

[61] G. P. Bryan-Brown, C. V. Brown, J. C. Jones, E. L. Wood, I. C. Sage, P. Brett, and J. Rudin, 5.3: Grating aligned bistable nematic device, Soc. Inf. Disp. Int. Symp. Dig. Tech. Pap. **28**, 37 (1997).

[62] A. Sengupta, Topological microfluidics: Present and prospects, Liq. Cryst. Today **24**, 70 (2015).

[63] A. M. Sonnet and E. G. Virga, *Dissipative Ordered Fluids: Theories for Liquid Crystals* (Springer, New York, 2012).

[64] F. M. Leslie, Theory of flow phenomena in liquid crystals, Adv. Liq. Cryst. **4**, 1 (1979).

[65] M. T. Viciosa, A. M. Nunes, A. Fernandes, P. L. Almeida, M. H. Godinho, and M. D. Dionísio, Dielectric studies of the nematic mixture E7 on a hydroxypropylcellulose substrate, Liq. Cryst. **29**, 429 (2002).

[66] E. Vicente Alonso, A. A. Wheeler, and T. J. Sluckin, Nonlinear dynamics of a nematic liquid crystal in the presence of a shear flow, Proc. R. Soc. London A **459**, 195 (2003).

[67] A. Romo-Uribe and A. H. Windle, "Log-rolling" alignment in main-chain thermotropic liquid crystalline polymer melts under shear: An in-situ WAXS study, Macromolecules **29**, 6246 (1996).

[68] D. Crowdy and H. Kang, Squeeze flow of multiply-connected fluid domains in a Hele-Shaw cell, J. Nonlinear Sci. **11**, 279 (2001).

[69] M. J. Shelley, F.-R. Tian, and K. Wlodarski, Hele-Shaw flow and pattern formation in a time-dependent gap, Nonlinearity **10**, 1471 (1997).

[70] A. D. Rey, Capillary models for liquid crystal fibers, membranes, films, and drops, Soft Matter **3**, 1349 (2007).

[71] *Physical Properties of Liquid Crystals: Nematics*, edited by G. R. Luckhurst, D. A. Dunmur, and A. Fukuda, INSPEC (Institution of Electrical Engineers, London, 2001).

[72] P. W. Benzie and S. J. Elston, Optics of liquid crystals and liquid crystal displays, in *Handbook of Visual Display Technology*, edited by J. Chen, W. Cranton, and M. Fihn (Springer, Berlin, 2012), Chap. 7.2.1, pp. 1365–1385.

[73] COMSOL Multiphysics, Version 5.5, http://www.comsol.com, COMSOL, Inc., Burlington MA, 2019.

[74] L. Tortora and O. D. Lavrentovich, Chiral symmetry breaking by spatial confinement in tactoidal droplets of lyotropic chromonic liquid crystals, Proc. Natl. Acad. Sci. USA **108**, 5163 (2011).

[75] D. Vanzo, M. Ricci, R. Berardi, and C. Zannoni, Wetting behaviour and contact angles anisotropy of nematic nanodroplets on flat surfaces, Soft Matter **12**, 1610 (2016).